NSF GRANT # DMI-0900138
NSF PROGRAM NAME: Control Systems Program

Hybrid Control of Continuous Casting for Whale and Crack Prevention and Resonance Control in Mold Oscillation System

Joseph Bentsman
University of Illinois, Department of Mechanical Science and Engineering

Brian G. Thomas, Bryan Petrus, Xiaoxu Zhou, Vivek Natarajan
University of Illinois, Department of Mechanical Science and Engineering

Ron O'Malley
Nucor Steel Decatur, AL

Abstract: A novel 1D spray-cooling control system is described that has been implemented on a commercial caster. The system provides the desired shell surface temperature by employing a hybrid open-loop/closed-loop shell surface temperature estimator, and proportional-integral controller. A 2D through-thickness temperature regulation is then addressed by deriving a full-state feedback control law that stabilizes the two-phase Stefan problem with respect to a reference solution using control of the Neumann boundary condition. A simple Dirichlet controller is also considered, and is used to design a boundary-output-based estimator that, in combination with full-state feedback controllers, yields a plausible output feedback control law with boundary sensing and actuation. Finally, a control approach is proposed for eliminating distortions in mold oscillation systems which are problematic in some continuous casters.

1. Introduction: Since its development in the mid 1980's, an increasing amount of the steel produced in the world has been made through thin-slab continuous casting. Thin-slab casting, defined here as slabs less than 100 mm thick, has faster casting speeds and is usually based on scrap. In this process, molten steel is poured into a water-cooled mold at the top of the caster, where a solid shell is formed around the liquid core. This partially solidified "strand" is then driven through the "secondary cooling" region, which has a series of rolls and water or water-mist sprays that contain and cool the strand until it is fully solidified into slabs. If the steel is not fully solidified when it leaves this containment region, the ferrostatic pressure causes the strand to bulge. This costly and possibly dangerous event is called a "whale."

The quality and profitability of this process are tied to increasing the speed at which the steel is made, while maintaining ideal cooling conditions for the strand. A thin-slab continuous caster at full capacity can make over 100 tons of steel an hour. At these speeds, automatic control is of great benefit, but faces a variety of practical and theoretical challenges due to the harsh environment, short required response times, and highly nonlinear nature of the processes. In this work, novel control methods have been applied to the continuous steel slab casters at the Nucor Steel mill in Decatur, Alabama. The first part of this paper (Sections 2 and 3) examines controlling the secondary cooling water sprays to prevent surface defects and whale formation. The second part (Section 4) examines controlling the oscillating mold.

Robust and accurate control of secondary cooling is vital to the production of high quality slabs [1]. Defects such as transverse surface cracks form unless the temperature profile down the caster is optimized to avoid excessive stress and strain, such as caused by unbending, during temperature regions of low ductility [2]. This is especially important in thin-slab casters, because high casting speed and a tight machine radius exacerbate cracking problems. Thus, there is great incentive to implement control systems to optimize spray cooling to maintain desired temperature profiles.

However, conventional feedback control systems based on hardware sensors have not been successful because emissivity variations from intermittent surface scale and the harsh, steam-filled environment make optical pyrometers unreliable. Most casters control spray-water flow rates using a simple look-up table based on casting speed, but this produces undesirable temperature transients during process changes. Recent dynamic control systems have been developed based on real-time computational models.

Early systems [3-6] updated slowly or had relatively crude models, due to limited computing speed. More recently, significant achievements have been made in open-loop model-based control systems for

conventional thick-slab casters [7-9], although none of the models are robust enough for general use, and none has been applied to a thin-slab caster.

Section 2 describes a new online control system, previously described in various publications [10-13], that has been developed based on a real-time model. A PI control bank uses the model as a hybrid open/closed-loop estimator to adjust the water sprays to maintain a desired surface temperature. Section 2 gives details on the various components of the system, and briefly describes the lessons learned from simulations and online testing of the system at Nucor Decatur.

The controller for that system is limited in two important ways: it only considers the surface temperature, and it is uses a standard PI control for a rather complex non-linear, infinite-dimensional system. Section 3 describes work that improves on the controller design by attempting full-state feedback control of a nonlinear partial differential equation (PDE) of a type known as a Stefan problem. This problem includes a moving boundary, and can be used to describe the melting of a pure material, or certain grades of steel. Previous work on control of Stefan problem includes numerical optimization methods [14, 15], solutions of the inverse Stefan problem [16-18], and feedback control methods [19-21]. The numerical optimization methods in [14] and [15] can take into account realistic metallurgical constraints and quality conditions. However, they cannot realistically run in real-time. The inverse methods and feedback control methods focus on control of the boundary position, which would ensure whale prevention, but not necessarily the steel quality. The inverse problem, as solved in [16] and [17] directly and in [18] by minimizing a cost functional, is very numerically complex and thus limited to design of open-loop controllers. The feedback control methods are better suited for real-time control, but the control in [19] and [20] is simplified to the "on-off" thermostat-style one. In [21], as well as in Section 2 of this work, PI controllers are designed based on a discretized form of the solidification evolution equations. However, neither controls the full temperature distribution. [21] only considers the solidification boundary, while Section 2 focuses on the steel surface temperature. In Section 3, we apply in a novel fashion a Lyapunov functional taking into account the moving boundary to find several control laws for the Stefan problem. The performance of these laws is examined both mathematically, and through numerical simulation.

In continuous casting of steel, the mold executes a sinusoidal vertical motion of specific frequency and amplitude, imposed by a mold oscillation system. Metallurgical considerations require the sinusoidal profiles of the mold displacement and the corresponding velocity to be undistorted [22]. The mold oscillation system in some casters consists of a subsystem of beams that supports a heavy mold (~25,000 Kg) at one end and is subject to sinusoidal motion by an electro-hydraulic servo actuator with piston attached to this subsystem at the other end, to drive the mold. The servo is open loop unstable and is typically operated under feedback. The desired mold displacement is specified as the actuator piston position reference. At frequencies that are submultiples of the first resonant frequency of the beams in the subsystem, a significant distortion is observed in the mold displacement profile. The goal is to identify the source of this submultiples distortion problem and eliminate it. This is addressed in Section 4 and the subsections therein. Section 4.1 introduces the simplified physical testbed while Section 4.2 presents the mathematical model of the testbed as a set of coupled nonlinear ODEs and PDEs. Section 4.3 presents the controller and Section 4.4 includes the numerical and experimental controller validation.

2. Model-based PI Control with Hybrid Observer:

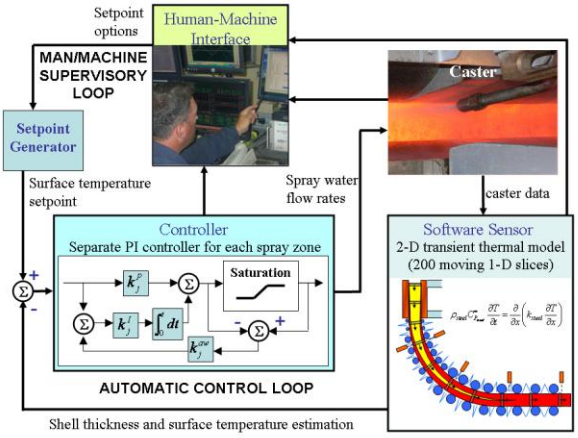

a) general overview

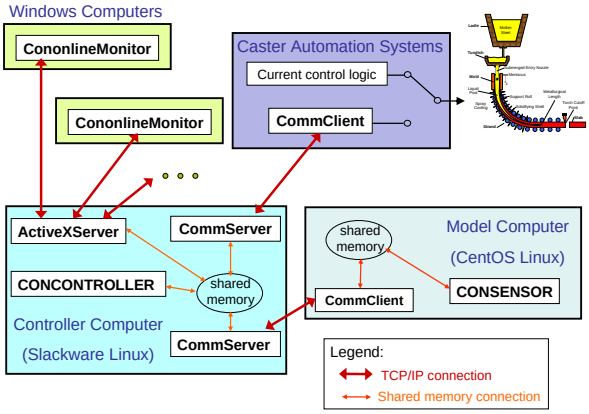

b) system overview

Figure 1: Schematics of CONONLINE system

As part of ongoing work with the Nucor Steel Decatur sheet steel mill, a new online control system has been developed, and described in various publications [10-13]. This system, called CONONLINE, has been implemented at the Nucor Steel casters in Decatur, Alabama. The system features a real-time solidification and heat-transfer model, CONSENSOR, of a longitudinal slice through the strand as a "software sensor" of surface temperature. A control algorithm, CONCONTROLLER, featuring a bank of proportional-integral (PI) controllers, uses this prediction to maintain the shell surface temperature profile at desired setpoints in each of the spray cooling zones through changes in casting conditions. Finally, a monitor interface provides real-time visualization of the shell surface temperature and thickness predictions, along with other information important to the operator, as well as to allow operator input through the choice of temperature setpoints.

An overview of the real-time control system is pictured in Figure 1a. It features a "software sensor" CONSENSOR, which estimates strand temperature in real time from available casting conditions for CONTROLLER, which evaluates the error with operator-generated setpoints and sends spray water flow rate "commands" to both the plant and CONSENSOR. Figure 1b shows the computing setup, as implemented at Nucor Decatur. The software sensor and controller run on separate servers for stability and speed reasons. The monitor program runs on Windows PCs to display the programs' outputs. The programs communicate using shared memory on each server and TCP/IP connections between the computers. Further details are given in [10] and [12].

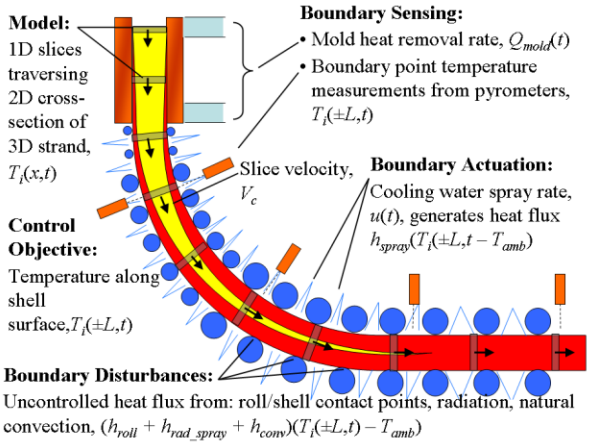

Figure 2. CONSENSOR slice diagram

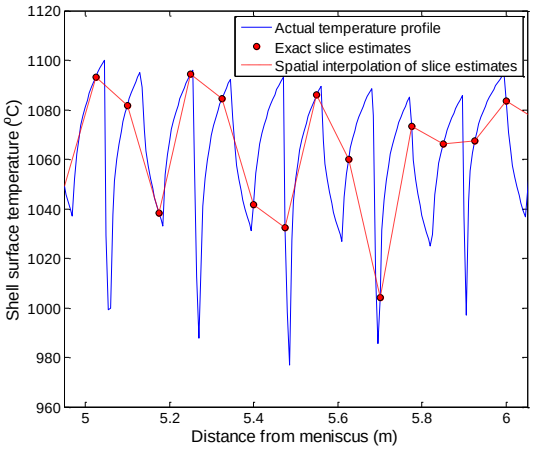

Figure 3. Slice interpolation

2.1. Software Sensor – CONSENSOR: At typical casting speeds, the continuously-cast strand has a high Peclet number, rendering axial heat conduction negligible. Hence, the temperature and solidification of the steel at any point in the strand can be predicted by modeling a "slice" of the material as it moves down through the caster at the casting speed. Focusing on the centerline of the strand, these slices are one-dimensional and the numerical calculations can be computed quickly using an explicit finite difference scheme [23]. By simulating and interpolating between multiple slices, as illustrated in Figure 2, the temperature of the strand is estimated in real-time.

The temperature in each slice is described by the 1-D transient heat conduction equation [23]:

$$\rho_{steel} Cp^*_{steel} \frac{\partial T(x,t)}{\partial t} = k_{steel} \frac{\partial^2 T(x,t)}{\partial x^2} + \frac{dk_{steel}}{dT}\left(\frac{\partial T(x,t)}{\partial x}\right)^2 \quad (1)$$

where k_{steel} is thermal conductivity, ρ_{steel} is density, and Cp^*_{steel} is the effective specific heat of the steel, which includes the latent heat based on liquid fraction via a modified Clyne-Kurz microsegregation model [23, 24]. The spatial dimension x extends through the entire thickness of the strand, perpendicular to the casting direction, to allow nonsymmetrical heat extraction. The initial condition is the pour temperature, measured in the tundish. Heat flux boundary conditions are applied based on plant measurements of cooling water flow rates and temperature rise for the mold, and heat transfer coefficients according to spray water flow rates for the secondary cooling region. More detail on this model is provided elsewhere [12, 23].

An offline computational model with these features was previously developed as the program CON1D. The accuracy of this model has been demonstrated through comparison with analytical solutions of plate solidification and plant measurements [23, 25]. Because of its accuracy, CON1D has been used in many previous studies to predict successfully the effects of

casting conditions on solidification and to develop practices to prevent problems such as whale formation [26].

The software sensor, CONSENSOR, uses CON1D as a subroutine to simulate individual slices, starting each slice simulation at the meniscus at different times to achieve a fixed spacing between the slices. This is illustrated in Figure 2 using N = 10 slices for simplicity. To assemble the complete temperature profile requires careful interpolation of the slice results. As illustrated in Figure 3, the span between slices can pass over the temperature dips and peaks caused by the roll and spray spacing, resulting in errors of 100 °C or more. This problem is overcome by "delay interpolation," estimating the temperature at each point in the caster at time t from the latest temperature available from the CON1D slice histories. This process is described in detail in [12].

The model was calibrated to match the average surface temperatures measured under steady-state conditions using five pyrometers installed in the south caster at Nucor Steel Decatur in January, 2006. An example comparison of the measurements and temperature predictions is shown in Fig 4. The predicted temperatures generally exceed those measured by the pyrometers, except for the last pyrometer, which is outside the spray chamber and expected to be most reliable. The difference is believed to be due to the pyrometers reading lower than the real temperature, owing to steam-layer absorption and surface emissivity problems. Further work is needed to improve the accuracy of the pyrometer measurements, the spray heat-transfer coefficients, the spray-zone lengths, and the predicted variations in surface heat transfer and temperature, in order to improve the agreement.

The shell thickness prediction has also been calibrated to match recorded whale events at the Nucor Decatur casters, as well as high casting speed conditions where containment was not lost.

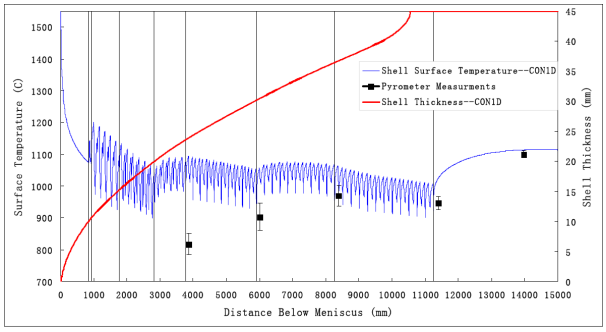

a) along entire domain

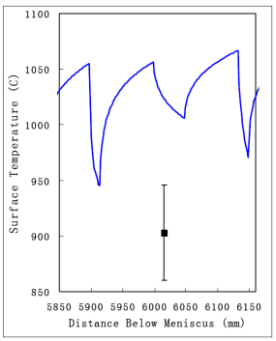

b) close-up near one roll spacing

Figure 4. Comparison of CON1D surface temperature predictions and measurements

2.2. Control Algorithm – CONCONTROLLER: In a continuous caster, rows of individual spray nozzles are grouped into "spray zones" based on how they are connected via headers and pipes to control valves. All rows of nozzles in a zone have the same spray-water flow rate and spray density profile. The spray rate for zone j is denoted below as u_j. CONCONTROLLER controls each zone with an independent PI controller, tuned separately to meet the desired control performance. CONSENSOR, as described above, only predicts the temperature along the center of the strand. Hence, CONCONTROLLER only applies PI control to zones covering the center. The spray flow rates for other zones across the strand width are prescribed as a function of slab width using separate logic.

At each time step t, the shell surface temperature profile estimate, $\hat{T}(z,t)$ where z denotes the casting direction, is obtained by CONSENSOR and the desired temperature profile $T^s(z,t)$, or setpoint, is determined as discussed below. The difference between the two is averaged over each zone j, giving the zone errors $\Delta T_j(t)$. Then the spray-water flow rate command for the next time interval is calculated via the classic PI control law:

$$u_j(t+\Delta t) = u_j^P(t+\Delta t) + u_j^I(t+\Delta t), \quad j = 1,\ldots,n_{zone}, \tag{2}$$

where the proportional and integral components are calculated respectively as:

$$u_j^P(t+\Delta t) = k_j^P \Delta T_j(t) \tag{3}$$

$$u_j^I(t+\Delta t) = u_j^I(t) + k_j^I \Delta T_j(t)\Delta t + \frac{1}{N_{aw}} \sum_{n=0}^{N_{aw}-1} \left[u_j^{measured}(t-n\Delta t) - u_j(t-n\Delta t) \right]. \tag{4}$$

The first part of (4) is a discrete-time integral over the time interval Δt. The summation term is an anti-windup [27] adjustment, adopted to avoid integrator windup when the control flow-rate commands are outside the limits on the possible flow rates through the valves. This tends to cause controller instability, known as

"windup". This problem is prevented by subtracting the difference between the measured spray rates and the controller-suggested spray rates from the integral in Eq. (4). This difference is averaged over N_{aw} time steps to filter out oscillations caused by chattering in the valves, as discussed below.

2.3. Combining CONSENSOR and CONCONTROLLER – Certainty Equivalence and Loop Closure Issues: The PID bank in the CONCONTROLLER system described above uses strand surface temperature in the secondary cooling region estimated by an observer (CONSENSOR model program) to define its output error: deviation from the desired temperature-profile setpoints. In control terminology, this is the "certainty equivalence principle" – using the estimate as if it were the true value.

The loop closure employed here, however, has some special features. In the mold, CONSENSOR performs closed-loop estimation, with the temperature estimate being quite accurate, because it is based on the measured mold heat removal rate and an accurate boundary heat flux profile. The estimated slice temperature profile at mold exit is referred to as an inferred measurement [28] because it is produced by a model from a secondary measurement. Due to the temperature continuity at mold exit, this inferred measurement becomes the initial condition for the slice prediction in the secondary cooling region. Hence, at the start of the secondary cooling region, the control system achieves inferential closed-loop control.

In the rest of the secondary cooling region, reliable real-time heat-transfer measurements are not possible, so the controller uses open-loop model-based temperature estimates. The quality of these estimates is still very good because in addition to being accurately initialized at mold exit, the model correctly incorporates the effects of several casting process changes (with casting speed, superheat, and grade the most important) on strand-temperature evolution from a fundamental basis and has been calibrated offline to correctly predict whale formation under a few typical conditions. However, several other process variations, such as hysteresis in the boiling heat transfer coefficients and spray-nozzle clogging, are not modeled in CONSENSOR. Without the ability to measure the strand surface temperature accurately and robustly in real time, surface temperature estimate accuracy could deteriorate with distance below mold exit.

This combination of closed-loop estimation localized at mold exit (i.e. spatially discrete) with open-loop estimation throughout the rest of the strand (i.e. spatially continuous) is strictly termed a hybrid discrete-continuous [29] closed-loop/open-loop observation of the strand temperature profile in the secondary cooling region. The resulting control system can thus be termed hybrid closed-loop/open-loop system, as well. Even if the placement of reliable pyrometers becomes technically feasible in the future, the pyrometer measurements are still essentially spatially discrete and strand temperature in the gaps between pyrometers would have to be estimated in the open loop. Hence, the control system would retain this hybrid nature. Since this reinforces the importance of modeling accuracy to ensuring estimator quality, lab measurement of heat transfer coefficients during air-mist spray cooling and further calibration with plant measurements is being addressed as another important aspect of the larger project.

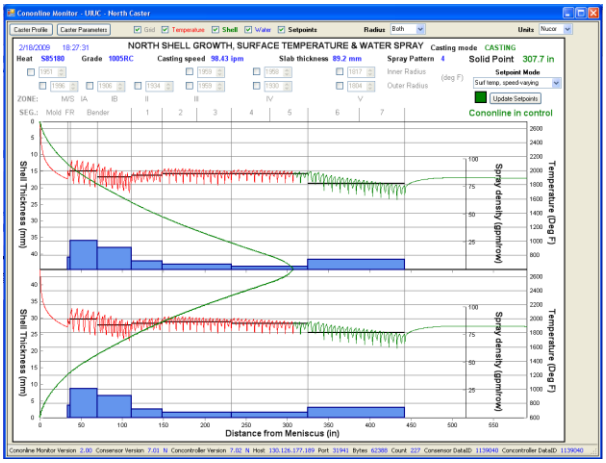

a) Profile screen

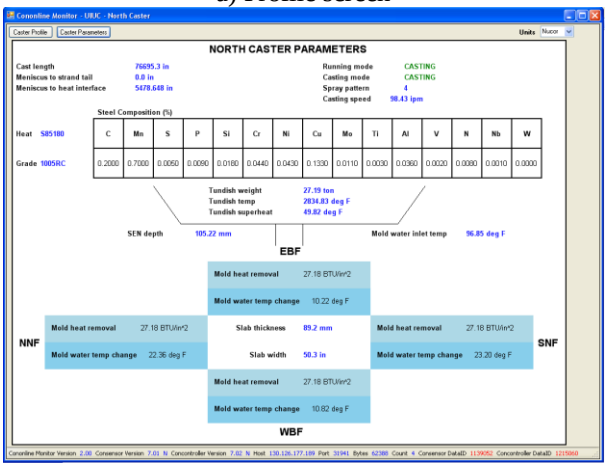

b) Parameter screen

Figure 5. CONONLINE Monitor interface screens

2.4. Visualization – CONONLINE Monitor: The monitor, as illustrated in Figure 1, is an important part of the system that provides real-time display of many variables, setpoints, and predictions, permitting operators and plant metallurgists to monitor the caster and the control system performance, and to make adjustments as needed. Figure 5 shows typical screen

shots of the two interface screens that the monitor can display.

Figure 5a shows the "profile screen," which serves two purposes. The first purpose is to relay key simulation outputs to the operators and plant engineers. It is also an interface for operator input to the controller, via controls for changing the temperature setpoint in any zone manually. Figure 5b shows the "parameter screen," which displays the most important caster measurements input to the model. This allows for easy checking of the casting conditions, and program statuses.

2.5. Setpoint Generation: Choosing a good setpoint profile $T^s(z,i)$ is as challenging and important as the control task itself. Traditional spray practice is based on "spray-table control." Spray flow rates for each zone that produce good quality steel in a specific caster are determined from plant trial and error and previous experience. Higher casting speeds require higher water flow rates to maintain the same cooling conditions, so a different spray profile is tabulated for several casting speeds in a database spanning the range of normal operation. This array of spray rates is organized by zone and casting speed, or "spray pattern," and may be different for differing grades of steel. During casting, spray setpoints are interpolated from the database, called a "spray table," for the chosen pattern and casting speed. This method does not accommodate transient behavior very well.

To take advantage of this available knowledge base, the spray table was converted to a table of surface temperature profile setpoints. For each pattern, CON1D was run at a typical casting speed (3.5 m/min for Nucor Decatur) using the water spray rates in the spray table. Therefore, each pattern has a corresponding temperature profile as the setpoint for the PI controller, $T^s(z,t)$. The automatic setpoints can also be over-ridden in any zone(s) using the monitor interface.

2.6. Simulation Results: The model and controller programs can be also used to simulate the caster response to changing casting conditions, and the monitor can be used to view the results graphically in real-time. For example, Figure 6 compares the zone-average surface-temperature histories extracted from the software sensor predictions in the fifth (next to last) spray zones below the meniscus during a sudden drop in casting speed from 3.0 m/min to 2.5 m/min at t = 30s. Figure 6b shows the respective spray rates assigned to each zone using 3 different control methods. Additional results from these simulations are available in [12].

If no change is made to the spray-water flow rates, the surface temperature eventually drops. With a controller that changes spray water flow rates in proportion to casting speed, during the sudden speed drop, all of the spray rates drop immediately. However, with the recently higher casting speed, the upstream steel is hotter than expected, so the temperature overshoots the steady-state value. The steady-state temperatures are higher at the lower speed because the spray rates assigned in the spray table are predicted by the model to drop even more than the drop in speed requires. Finally, with PI control, the surface temperature is kept remarkably constant through the speed change. The spray flow rates decrease more gradually after the casting speed change. Furthermore, the flow rates lower in the caster drop more gradually than those nearer to mold exit (not shown). Steady state is not reached until steel starting at the meniscus at the transition time finally reaches the given point in the caster, after being cast entirely under the new conditions.

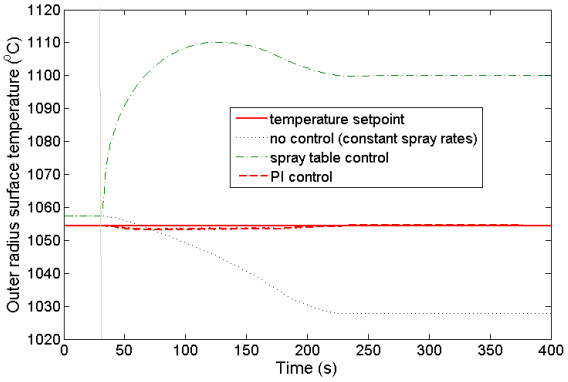

a) Zone-average outer radius surface temperature

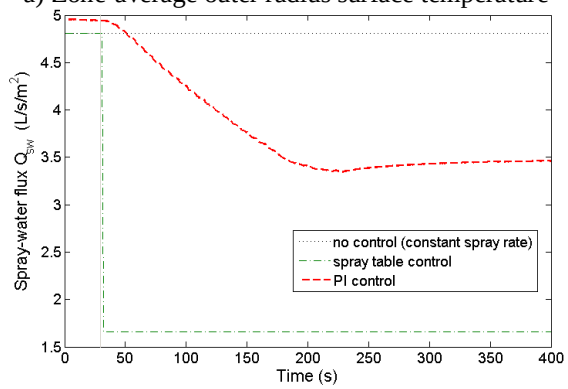

b) Spray water flow rates

Figure 6. Results of offline simulation of slowdown, comparing control methodologies

This case study demonstrates that all of the controllers perform as expected. The PI controller produces the best response for steel quality, as detrimental surface temperature fluctuations are lessened. The quality of the control system now depends on the accuracy of the software sensor calibration to match the real caster. Work is proceeding to measure heat transfer, both with

fundamental laboratory experiments, and with optical pyrometers and other experiments in the commercial steel thin-slab caster.

2.7. Implementation at Nucor Steel Decatur: The real-time CONSENSOR model has been running on servers at the Nucor Decatur sheet steel mill since 2006. Since 2008, dedicated workstations have been set up in the caster pulpit to run monitors for each of the two casters, which are called North and South caster at the mill. During this time, the system was run in "shadow mode," in which temperature and shell predictions are supplied to operators through the monitor, but the system does not control the water sprays. At first, the system was only installed on the North Caster. During this time, a whale event occurred on the South caster, while on the North caster operators used the visual prediction of the liquid core to reduce casting speed as needed to prevent loss of containment. The operators immediately requested the system also be installed on the South caster.

Several successful tests with CONONLINE in control of the water sprays have been performed, up to several hours in length. In addition to model calibration, changes have been made to the control algorithm to resolve issues noticed during the tests. In particular, the controller gains were made less aggressive when it was found that the spray valve system had a longer time constant than was anticipated. Also, the valves had some chattering that lead to sinusoidal noise in the spray rates. The classical anti-windup method, equivalent to Eq. (4) with N_{aw} = 1, transmitted these oscillations to the control signal. To prevent this, the oscillations were filtered out by averaging the anti-windup signal over time. The controller also sometimes called for sharp changes in spray rate in the first few spray zones, due to significant variations in strand surface temperature at mold exit caused by changes in mold heat flux, casting speed, and steel grade. To avoid this problem, the temperature setpoint for the first spray zone is now half-way between the surface temperature at mold exit and the setpoint for the second zone.

Finally, it has been found that additional logic is needed to deal with unusual casting conditions. In particular, Nucor Decatur has a breakout prevention system that sometimes slows down the casting speed to 0.25 m/min when thermocouple readings in the mold indicate a thin spot. However, since CONSENSOR uses average mold heat removal, it does not predict the highly localized thin spot. As illustrated above, PI control would lower the spray rates during sudden slowdowns, which could cause the thin spot to break out. Instead, during these so-called "sticker slowdowns," CONCONTROLLER has been adjusted to override PI control in the first three spray zones with default minimum sprays based on the spray table. Similar efforts are continuing to help with casting startups and tailouts. Once resolved, the plan is for CONONLINE to take over permanent control of the casters.

3. Distributed-parameter-based feedback control of the two-phase Stefan problem: The work above is focused on ensuring surface temperature regulation. This is important to preventing transverse surface cracks, which may occur when the surface temperature is in the so-called "ductility trough" region in the bending or unbending regions of the caster. This does not give a guarantee of whale prevention in general conditions, which depends on ensuring the temperature throughout the thickness is below the melting temperature by the end of containment. Moreover, the controller above is finite-dimensional applied to a process that is inherently infinite-dimensional. Hence, parallel to the work described in Section 2, we have devised control laws based on a distributed parameter model of the temperature in the solidifying steel.

Instead of Eq. (1), we consider a model of the solidifying steel as a non-linear partial differential equation (PDE) of the form commonly known as a Stefan problem. This problem divides the domain into two or more time-varying subdomains separated by moving boundaries. In the casting process, these domains correspond to the solid and liquid phases of the material. The movement of the boundary between the phases is described by the Stefan condition, a differential equation derived from an energy balance at the boundary that is a function of the left and the right spatial derivatives of the temperature at the boundary [30]. This model is less general than Eq. (1), and is most accurate for pure iron and ultra-low carbon (ULC) steels. However, it is linear within each sub-domain, which allows for greater tractability for control design.

3.1. Problem Description: Using the same reasoning as in Section 2, the temperature evolution equations for the centerline of the strand may be reduced to a one-dimensional moving slice. Here, we assume the slice temperature is symmetric, and only consider the region between the strand surface and center.

We denote the temperature within the slice as $T(x,t)$, with $0 \le x \le L$ and $t \ge 0$, where $x = 0$ and $x = L$ correspond to the outer surface and the center of the strand, respectively. The position of the boundary between solid and liquid phases is denoted as $s(t)$. Then the following partial differential equation models the evolution of temperature within the slice:

$$T_t(x,t) = aT_{xx}(x,t),\ 0 < x < s(t),\ s(t) < x < L,$$
$$T(s(t),t) = T_f, \tag{5}$$
$$T_x(0,t) = u(t),\quad T_x(L,t) = 0,\ T(x,0) = T_0(x),$$
$$\dot{s}(t) = b\left(T_x\left(s^-(t),t\right) - T_x\left(s^+(t),t\right)\right),\ s(0) = s_0. \tag{6}$$

In physical terms, T_f is the melting temperature, a is the thermal diffusivity, and $b = k/\rho L_f$, where k is the thermal conductivity, ρ is the density, and L_f is the latent heat of fusion. All of these physical quantities are strictly positive. The control input $u(t)$ is applied as the left-hand side Neumann boundary condition. In the continuous caster, this is directly proportional to the heat flux removed from the steel at the surface.

For the convergence proof, we will need the following assumptions on the initial conditions:

(A1) $0 < s_0 < L$ and $T_0(s_0) = T_f$, $T(x,t) < T_f$ for $0 \le x < s(t)$, and $T(x,t) \ge T_f$ for $s(t) \le x \le L$

(A2) $T_0(x)$ is continuous on $[0,L]$ and infinitely differentiable except at s_0.

The assumptions, respectively, ensure that the equations are well defined at $t = 0$ and that solutions have sufficient regularity. Throughout this paper, we deal with the case in which $\varepsilon < s(t) < L - \varepsilon$ for some $\varepsilon > 0$, that is when the slice is neither fully solid nor liquid and the Stefan problem is well defined. We note that if this is not true, the problem is linear and may be dealt with using known distributed parameter control methods, e.g. those in [31].

3.2. Reference System and Error: We assume that we have a known reference temperature $\bar{T}(x,t)$ and solidification front position $\bar{s}(t)$, that are the solutions to (5)-(6) under known reference control input $\bar{u}(t)$ with initial conditions $\bar{T}(x,0) = \bar{T}_0(x)$ and $\bar{s}(0) = \bar{s}_0$ satisfying assumptions (A1) and (A2). This reference temperature profile should satisfy the metallurgical goals and constraints of the process, and could, for example, be calculated for the continuous caster via the optimization methods of [14, 15] or the inverse methods of [16-18]. Another obvious source for these reference temperatures is from the current spray table practices described in Section 2.5. That is, matching the reference temperature should result in safe operation and good quality steel. We add one more assumption on the reference profile:

(A3) $\dot{\bar{s}}(t) > 0$ for all $t \ge 0$.

We denote the reference errors as $\tilde{T}(x,t) = T(x,t) - \bar{T}(x,t)$, and $\tilde{s}(t) = s(t) - \bar{s}(t)$. Also denote $\tilde{u}(t) = u(t) - \bar{u}(t)$. Subtracting the PDEs yields

$$\tilde{T}_t(x,t) = a\tilde{T}_{xx}(x,t),\ x \in (0,L)\setminus\{s,\bar{s}\}. \tag{7}$$

Also, since solutions to (5) are twice spatially differentiable outside of the solidification front, they must have continuous first spatial derivatives. Thus, if $\bar{s}(t) \ne s(t)$, then $\bar{T}_x\left(s^+(t),t\right) = \bar{T}_x\left(s^-(t),t\right)$, and so

$$\dot{s}(t) = b\left(\tilde{T}_x\left(s^-(t),t\right) - \tilde{T}_x\left(s^+(t),t\right)\right). \tag{8}$$

Similarly,

$$\dot{\tilde{s}}(t) = -b\left(\tilde{T}_x\left(\bar{s}^-(t),t\right) - \tilde{T}_x\left(\bar{s}^+(t),t\right)\right). \tag{9}$$

In the remainder of this section, we will employ a simplified notation, using $T(x)$ to represent $T(x,t)$, or omitting both arguments altogether.

3.3. Control Law: The main result of this section is stated as follows:

Theorem 1. Let the system (5)-(6) be controlled such that

$$\begin{aligned} u(t) = \bar{u}(t) - \frac{1}{\tilde{T}(0) + \tilde{T}_{xx}(0)}\Bigg[&\tilde{T}_x(x)\left(\tilde{T}(x) + \tilde{T}_{xx}(x)\right)\Big|_{s^-}^{s^+} \\ &+ \tilde{T}_x(x)\left(\tilde{T}(x) + \tilde{T}_{xx}(x)\right)\Big|_{\bar{s}^-}^{\bar{s}^+} + \frac{1}{2a}\dot{s}(t)\tilde{T}_x^2(x)\Big|_{s^-}^{s^+} \\ &+ \frac{1}{2a}\dot{\bar{s}}(t)\tilde{T}_x^2(x)\Big|_{\bar{s}^-}^{\bar{s}^+}\Bigg] \end{aligned} \tag{10}$$

where the initial conditions satisfy (A1) and (A2), and the reference solidification front position satisfies (A3). Then the reference error $\tilde{T}(x,t)$ converges uniformly to 0 as $t \to \infty$.

Proof: Consider the Lyapunov functional

$$\begin{aligned} V(\tilde{T}) := \frac{1}{2}\int_0^L\left(\tilde{T}^2 + \tilde{T}_x^2\right)dx = \frac{1}{2}\Bigg[&\int_0^{s_1}\left(\tilde{T}^2 + \tilde{T}_x^2\right)dx \\ &+ \int_{s_1}^{s_2}\left(\tilde{T}^2 + \tilde{T}_x^2\right)dx + \int_{s_2}^{L}\left(\tilde{T}^2 + \tilde{T}_x^2\right)dx\Bigg], \end{aligned} \tag{11}$$

where $s_1 := \min\{s,\bar{s}\}$ and $s_2 := \max\{s,\bar{s}\}$. Note that $V(\tilde{T})$ is equivalent to the square of the Sobolev norm,

$$\left\|\tilde{T}\right\|_{1,2} := \left\|\tilde{T}\right\|_2 + \left\|\tilde{T}_x\right\|_2, \tag{12}$$

in the sense that

$$\frac{1}{2}\left\|\tilde{T}\right\|_{1,2}^2 \ge V(\tilde{T}) \ge \frac{1}{4}\left\|\tilde{T}\right\|_{1,2}^2. \tag{13}$$

Since solutions of the Stefan problem are continuous and twice differentiable except at the boundary, the first weak derivative exists and such solutions are in the Sobolev space $W^{1,2}(0,L)$.

Assuming that $s(t) \neq \tilde{s}(t)$, and ignoring the degenerate case for now, the time derivative of (11) is given by:

$$\dot{V}(\tilde{T},t) = \frac{1}{2}\left(\tilde{T}^2(s_1^-) + \tilde{T}_x^2(s_1^-)\right)\dot{s}_1 + \frac{1}{2}\Big[\left(\tilde{T}^2(s_2^-) + \tilde{T}_x^2(s_2^-)\right)\dot{s}_2 - \left(\tilde{T}^2(s_1^-) + \tilde{T}_x^2(s_1^-)\right)\dot{s}_1\Big] - \frac{1}{2}\left(\tilde{T}^2(s_2^-) + \tilde{T}_x^2(s_2^-)\right)\dot{s}_2 + \int_0^{s_1}\left(\tilde{T}\tilde{T}_t + \tilde{T}_x\tilde{T}_{xt}\right)dx + \int_{s_1}^{s_2}\left(\tilde{T}\tilde{T}_t + \tilde{T}_x\tilde{T}_{xt}\right)dx + \int_{s_2}^{L}\left(\tilde{T}\tilde{T}_t + \tilde{T}_x\tilde{T}_{xt}\right)dx.$$

Inserting the PDE from (7) yields:

$$\dot{V}(\tilde{T},t) = -\frac{1}{2}\dot{s}_1\left(\tilde{T}^2(x) + \tilde{T}_x^2(x)\right)\Big|_{s_1^-}^{s_1^+} - \frac{1}{2}\dot{s}_2\left(\tilde{T}^2(x) + \tilde{T}_x^2(x)\right)\Big|_{s_2^-}^{s_2^+} + \int_0^{s_1}\left(\tilde{T}\tilde{T}_{xx} + \tilde{T}_x\tilde{T}_{xxx}\right)dx + \int_{s_1}^{s_2}\left(\tilde{T}\tilde{T}_{xx} + \tilde{T}_x\tilde{T}_{xxx}\right)dx + \int_{s_2}^{L}\left(\tilde{T}\tilde{T}_x + \tilde{T}_x\tilde{T}_{xxx}\right)dx.$$

We note here that the expression above contains the third spatial derivative. Since T and $\tilde{T}$ are solutions to the parabolic heat equation on the time-varying domains $(0,s)\cup(s,L)$ and $(0,\bar{s})\cup(\bar{s},L)$, respectively, they will be at least three times differentiable, as shown in Lemma 1 in the appendix. Therefore, $\tilde{T}$ will also have the third spatial derivative except at the boundary points.

Now, integrating by parts,

$$\dot{V}(\tilde{T},t) = -\frac{1}{2}\dot{s}_1\left(\tilde{T}^2(x) + \tilde{T}_x^2(x)\right)\Big|_{s_1^-}^{s_1^+} - \frac{1}{2}\dot{s}_2\left(\tilde{T}^2(x) + \tilde{T}_x^2(x)\right)\Big|_{s_2^-}^{s_2^+} + a\left(\tilde{T}\tilde{T}_x + \tilde{T}_x\tilde{T}_{xx}\right)\Big|_0^{s_1} - a\int_0^{s_1}\left(\tilde{T}_x^2 + \tilde{T}_{xx}^2\right)dx + a\left(\tilde{T}\tilde{T}_x + \tilde{T}_x\tilde{T}_{xx}\right)\Big|_{s_1}^{s_2} - a\int_{s_1}^{s_2}\left(\tilde{T}_x^2 + \tilde{T}_{xx}^2\right)dx + a\left(\tilde{T}\tilde{T}_x + \tilde{T}_x\tilde{T}_{xx}\right)\Big|_{s_1}^{L} - a\int_{s_1}^{L}\left(\tilde{T}_x^2 + \tilde{T}_{xx}^2\right)dx.$$

Then, applying the boundary conditions from (5) and combining like terms gives

$$\dot{V}(\tilde{T},t) = -a\int_0^L\left(\tilde{T}_x^2 + \tilde{T}_{xx}^2\right)dx - a\tilde{u}(0)\left(\tilde{T}(0) + \tilde{T}_{xx}(0)\right) - a\tilde{T}_x(x)\left(\tilde{T}(x) + \tilde{T}_{xx}(x)\right)\Big|_{s_1^-}^{s_1^+} - a\tilde{T}_x(x)\left(\tilde{T}(x) + \tilde{T}_{xx}(x)\right)\Big|_{s_2^-}^{s_2^+} - \frac{1}{2}\dot{s}_1\tilde{T}_x^2(x)\Big|_{s_1^-}^{s_1^+} - \frac{1}{2}\dot{s}_2\tilde{T}_x^2(x)\Big|_{s_2^-}^{s_2^+}.$$

Hence, if the control $u(t)$ satisfies (10), then

$$\dot{V}(\tilde{T},t) \leq W(\tilde{T}) := -a\int_0^L\left(\tilde{T}_x^2 + \tilde{T}_{xx}^2\right)dx \leq 0. \quad (14)$$

In fact, we have equality of the two functions for the usual case, but now we consider the degenerate case, in which $\bar{s}(t) = s(t)$ for some time interval of length greater than zero. This means $\tilde{T}(s(t),t) = 0$ in this interval, and since the boundaries move as governed by (6),

$$\begin{aligned} T_x(s^-) - T_x(s^+) &= \bar{T}_x(s^-) - \bar{T}_x(s^+) \\ \Rightarrow \tilde{T}_x(s^+) &= \tilde{T}_x(s^-) =: \tilde{T}(s). \end{aligned} \quad (15)$$

Then (10) simplifies to

$$u(t) = \bar{u}(t) - \frac{2\tilde{T}_x(s)}{\tilde{T}(0) + \tilde{T}_{xx}(0)}\tilde{T}_{xx}(x)\Big|_{s^-}^{s^+}.$$

Using these relationships and (7), we can again take the time derivative of (11), which in the degenerate case only has a single boundary. After integrating by parts,

$$\dot{V}(\tilde{T},t) = -a\int_0^L\left(\tilde{T}_x^2 + \tilde{T}_{xx}^2\right)dx + a\tilde{T}_x(s)\tilde{T}_{xx}(x)\Big|_{s^-}^{s^+}. \quad (16)$$

If $\tilde{T}_x(s) = 0$, then (14) clearly holds. If $\tilde{T}_x(s) > 0$, then for all $\varepsilon > 0$ sufficiently small, $T(s+\varepsilon) > 0$. If $\tilde{T}_{xx}(s) > 0$, then by (7), $\tilde{T}_t(s+\varepsilon) > c > 0$ for all $\varepsilon > 0$ sufficiently small. This means $\tilde{T}(s(t)+\varepsilon, t+\delta) > 0$ for all $\delta > 0$ sufficiently small. But, by assumption (A3), within the degenerate time interval,

$$s(t+\delta) = \bar{s}(t+\delta) > \bar{s}(t) = s(t) \Rightarrow s(t+\delta) = s(t) + \varepsilon$$

for some $\varepsilon > 0$. This means, taking δ small enough,

$$0 = \tilde{T}(s(t+\delta), t+\delta) = \tilde{T}(s(t)+\varepsilon, t+\delta) > 0.$$

By contradiction, then, $\tilde{T}_{xx}(s) \leq 0$. Similarly, $\tilde{T}_{xx}(s) \geq 0$. Therefore,

$$a\tilde{T}_x(s)\tilde{T}_{xx}(x)\Big|_{s^-}^{s^+} \leq 0$$

and (14) follows from (16). The same argument holds under reversed signs in the case $\tilde{T}_x(s) < 0$. Thus, in the degenerate case, under the given control law, the estimate (14) is still valid.

As an immediate conclusion of (13) and (14), under this control law the reference error $\tilde{T}$ is bounded in the $W^{1,2}(0,L)$ Sobolev norm.

We now apply an invariance principle for general evolution equations from [32]. Define the spaces $X = W^{1,2}(0,L)$ and $Y = C^0(0,L)$, and let $f(x)$ be an admissible initial value for the reference error. That is, $f(x) = T_0 - \bar{T}_0$ where T_0 and $\bar{T}_0$ satisfy assumptions (A1) and (A2). Define $G := \gamma(f) := \bigcup_{t\geq 0}\{S(t)f\}$ where $S(t)f$ is the solution to the error equations under the given control law. Since solutions to the Stefan problem are continuous and piecewise-C^2, $G \subset X$, and by Lemma 2 in the appendix, X is compactly embedded in Y. Therefore, G is compactly embedded in Y and, as noted above, G is X-bounded. Define

$$\hat{V}(y) := \int_0^L\left(\tilde{T}^2 + \tilde{T}_x^2\right)dx \text{ and } \hat{W}(y) := a\int_0^L\left(\tilde{T}_x^2 + \tilde{T}_{xx}^2\right)dx$$

to be, respectively, the extensions of V and W (defined in (14)) to $Cl_\gamma G$, the closure of G in the supremum norm. Since functions in G will be twice differentiable almost everywhere, both of these functionals are well defined, positive semi-definite, and lower semi-continuous on $Cl_\gamma G$. Thus, all the conditions of Theorem 6.3, p. 195, in [32] are met, giving the following result:

$$\lim_{t\to\infty} d_y\left(S(t)f, M_3\right) = 0 \tag{17}$$

where

$$M_3 := \left\{ y \in Cl_Y G : \hat{W}(y) = 0 \right\}.$$

In general, $M_3 = \left\{ \tilde{T}(x) : \tilde{T}_x(x) \equiv 0 \equiv \tilde{T}_{xx}(x) \right\}$, that is $T(x) = \bar{T}(x) + C$ for some constant C. So, consider any constant element $\tilde{T}(x) \equiv C$ in G. If $C \neq 0$, then $s \neq \bar{s}$, but since T is continuously differentiable except at s,

$$\bar{T}_x\left(\bar{s}^+\right) = T_x\left(\bar{s}^+\right) = T_x\left(\bar{s}^-\right) = \bar{T}_x\left(\bar{s}^-\right).$$

Then by (6),

$$\dot{\bar{s}} = -b\left(\bar{T}_x\left(\bar{s}^+\right) - \bar{T}_x\left(\bar{s}^-\right)\right) = 0.$$

This contradicts assumption (A3). This means that $M_3 \cap G = \{0\}$, and since $M_3 \subset Cl_\gamma G$, $M_3 = \{0\}$. Therefore, (17) is equivalent to

$$\lim_{t\to\infty} \left\| \tilde{T}(x,t) \right\|_\infty = 0. \quad \square$$

Remark 1. It does not follow from Theorem 1 that the solidification front position converges as well. If the temperature gradient in the reference profile is small, the solidification front position error may be arbitrarily large for small temperature errors. For practical applications, though, this gradient is not small, and the solidification front converges to the reference position as illustrated in the simulations in Section 3.6.

Remark 2. The well-posedness of the 1-D Stefan problem has been examined in depth, e.g. in [30, 33, 34], typically requiring boundedness of the boundary conditions and their time derivatives. The control law (10) may be unbounded, and therefore it may be necessary to regularize it in order to prove the general well-posedness of the closed-loop system. In the simulations, some regularity is attained by bounding the control, which does not result in the loss of convergence. A rigorous analysis of this issue will be carried out in subsequent work.

Remark 3. The presence of the second spatial derivative of the temperature error in the control law (10) ensures error convergence by inducing the relatively strong $W^{1,2}(0,L)$ Sobolev norm topology, but it also places additional smoothing requirements on the measurements. Relaxing the topology and removing the second spatial derivative yields a second control law given below that only depends on the first spatial derivative. However, it is only proven to be stable relative to the reference temperature, with the convergence conjectured based on given simulation results.

Theorem 2. Let the system (5)-(6) be controlled such that

$$\begin{aligned} u(t) &= \bar{u}(t) + \frac{1}{b\tilde{T}(0)}\left[\dot{s}\tilde{T}(s) - \dot{\bar{s}}\tilde{T}(\bar{s})\right] \\ &= \bar{u}(t) - \frac{1}{\tilde{T}(0)}\left[\tilde{T}(s)\tilde{T}_x(x)\Big|_{s^-}^{s^+} - \tilde{T}(\bar{s})\tilde{T}_x(x)\Big|_{\bar{s}^-}^{\bar{s}^+}\right] \end{aligned} \tag{18}$$

where the initial conditions satisfy (A1) and (A2). Then, the reference error $\tilde{T}(x,t)$ is bounded in the L^2 norm.

Proof: Consider the Lyapunov functional

$$\begin{aligned} V(\tilde{T}) &:= \frac{1}{2}\int_0^L \tilde{T}^2 dx = \frac{1}{2}\left\|\tilde{T}\right\|_2^2 \\ &= \frac{1}{2}\int_0^{s_1} \tilde{T}^2 dx + \frac{1}{2}\int_{s_1}^{s_2} \tilde{T}^2 dx + \frac{1}{2}\int_{s_2}^{L} \tilde{T}^2 dx, \end{aligned} \tag{19}$$

where $s_1 := \min\{s, \bar{s}\}$ and $s_2 := \max\{s, \bar{s}\}$. As in Theorem 1, we take the time derivative and integrate by parts, substituting in the PDEs and boundary conditions where appropriate. The result is

$$\begin{aligned} \dot{V}(\tilde{T},t) &= -a\int_0^L \tilde{T}_x^2 dx - a\tilde{u}(t)\tilde{T}(0) \\ &\quad - a\tilde{T}_x(x)\Big|_{s_1^-}^{s_1^+}\tilde{T}(s_1) - a\tilde{T}_x(x)\Big|_{s_2^-}^{s_2^+}\tilde{T}(s_2) \\ &= -a\left[\int_0^L \tilde{T}_x^2 dx - \tilde{u}(t)\tilde{T}(0) + \frac{1}{b}\dot{s}\tilde{T}(s) - \frac{1}{b}\dot{\bar{s}}\tilde{T}(\bar{s})\right]. \end{aligned}$$

If the control satisfies (18),

$$\dot{V}(\tilde{T},t) = -a\int_0^L \tilde{T}_x^2 dx \le 0. \tag{20}$$

In the degenerate case $s = \bar{s}$, control law (18) reduces to $u = \bar{u}$. Again taking the time derivative and integrating by parts gives (20), where the boundary terms drop out because $\tilde{u} = 0$ and $\tilde{T}(s) = \tilde{T}(\bar{s}) = 0$. Therefore, $V(\tilde{T})$, and consequently $\left\|\tilde{T}\right\|_2$, is bounded over time. $\square$

Although the proof does not guarantee convergence, the control law in simulation has shown convergent behavior as described in Section 3.6. Therefore, we formulate the following conjecture.

Conjecture 1. Let the system (5)-(6) be controlled such that $u(t)$ is given by (18) where the initial conditions

satisfy (A1) and (A2) and the reference temperature history satisfies (A3). Then, the reference error $\tilde{T}(x,t)$ converges in the L^p norm, $p \le 2$, to an ε-neighborhood of zero reference error.

A plausible proof could be based on the results in [32] as in Theorem 1, or use Barbalat's Lemma. Either method would require showing that $\|\tilde{T}_x\|_2$ is bounded along trajectories of the error system under control (18).

3.4. Applicability of the Control Law: Assumptions (A1) and (A2) will be true for all physically possible initial conditions. Assumption (A3) is generally true for any practical reference profile. An alternative to (A3) ensuring convergence to the reference system is:

(A4) The initial conditions satisfy $T_0(x) = T_f$ for $x \ge s_0$, and $\bar{T}_0(x) = T_f$ for $x \ge \bar{s}_0$.

Under this assumption, from the boundary conditions at $x = s(t)$ and $x = L$, it follows that $\tilde{T}(x) = 0$ for $x \ge s_2$ and all $t \ge 0$. This means $M_3 \cap G = \{0\}$ in the proof of Theorem 1, and the conclusion still holds.

There are two ways in which the model given by (5)-(6) significantly differs from the physical system. First, we assume arbitrary cooling and heating are available, when in fact control is limited to the cooling water sprays that are staggered with containment rolls in the caster and have spatially varying footprints. Moreover, the possible spray water flow rates are strictly limited by the spray piping system, and so saturation plays an important role. Although the proofs in Section 3.3 do not investigate the effects of saturation, we place bounds on the control signals in simulations in Section 3.6 and conjecture that the controlled system converges for initial conditions in a neighborhood in $W^{1,2}(0,L)$ of zero reference error.

Second, we have assumed full state feedback is available. It is clear that in the real process the temperature at any point below the surface cannot be measured. An important area for future improvement of this work, then, is in output feedback design, which is briefly addressed in the next section.

3.5. Dirichlet Control and Estimator Design: We now consider the case in which only the surface temperature can be measured, for example by optical pyrometers in the continuous caster. As before, the goal is to track a reference temperature history for the entire slice interior. First, we consider a controller in which the boundary surface temperature can be set exactly equal to the reference.

Theorem 3. Let the reference and the actual temperatures satisfy assumptions (A1), (A2), and (A4). In addition assume that $T_0(x) < T_f$ for $x < s_0$ and $\bar{T}_0(x) < T_f$ for $x < \bar{s}_0$, and that $\bar{T}(0,t) < T_f$ for all time. If the system (5)-(6) is controlled such that

$$T(0,t) = \bar{T}(0,t) \tag{21}$$

for all time, then the reference error $\tilde{T}(x,t)$ is bounded in the L^2 norm.

Proof: Under these assumptions, applying the maximum principle for parabolic equations, $T(x,t) < T_f$ for all $x < s(t)$. This means that $T_x(s^-) < 0$, and noting the signs in (6), $\dot{s} < 0$ for all time. The same holds for $\bar{T}$ and $\bar{s}$.

Again we use (19) as a Lyapunov functional candidate, and take the time derivative. Integrating by parts and applying the boundary conditions,

$$\dot{V}(\tilde{T},t) = -a\left[\int_0^L \tilde{T}_x^2 dx + \frac{1}{b}\dot{s}\tilde{T}(s) - \frac{1}{b}\dot{\bar{s}}\tilde{T}(\bar{s})\right].$$

Symbol	Description	Value
a	thermal diffusivity	3.98 x 10^{-6} W/m·K
b	Stefan condition constant	1.102 x 10^{-8} m^2/K·s
T_f	melting temperature	1783 K
L	half-thickness of strand	0.1 m

Table 1. Thermodynamic properties used in section 3.6 simulations

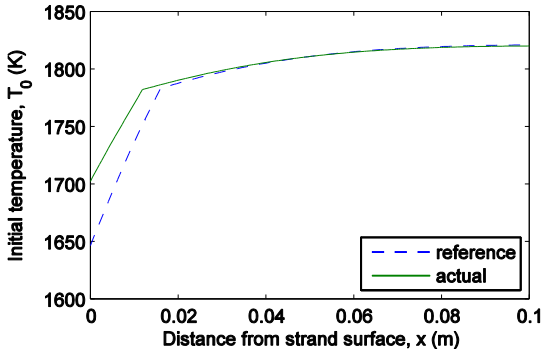

Figure 7. Initial temperature profiles for reference temperature $\bar{T}_0$ and actual temperature T_0.

Under assumption (A4), if $s > \bar{s}$, then $T(\bar{s}) = \bar{T}(s) = T_f$, and from above, $T(\bar{s}) < T_f = \bar{T}(s)$. This means $\dot{s}\tilde{T}(s) = 0$ and $\dot{\bar{s}}\tilde{T}(\bar{s}) < 0$. Similarly, if $s < \bar{s}$, then $\dot{s}\tilde{T}(s) > 0$ and $\dot{\bar{s}}\tilde{T}(\bar{s}) = 0$. In the degenerate case $s = \bar{s}$, the boundary terms drop out because $\tilde{T}(s) = \tilde{T}(\bar{s}) = 0$. In either case,

$$\dot{V}\left(\tilde{T},t\right) \le -a\int_0^L \tilde{T}_x^2 dx \le 0,$$

and thus $\left\|\tilde{T}\right\|_2$, is bounded over time. □

The weaknesses of this result compared to Theorem 1 are the lack of the convergence proof, the use of Dirichlet rather than heat flux boundary condition, and the use of the less accurate assumption (A4). However, it seems reasonable to conjecture as with Theorem 2 that there is some convergence, despite the lack of proof. Also, since the surface temperature is strongly affected by the heat flux due to the cooling water sprays, the Dirichlet boundary condition (21) can often be achieved in practice. The work in Section 2 is one method of achieving this goal, although some additional work is needed to account for the estimator uncertainty and PI controller delay. The strength of this result is that it only requires knowledge of $T\left(0,t\right)$, which can realistically be measured. Theorem 3 also immediately gives a possible estimator design.

Corollary 1. Define the feedback-based estimates $\hat{T}\left(x,t\right)$ and to be a solution to (5)-(6) with the Dirchlet boundary condition, based on boundary measurement of the plant, $\hat{T}\left(0,t\right)=T\left(0,t\right)$. Then, if T and $\hat{T}$ satisfy assumptions (A1), (A2), and (A4), and for all times t, $T\left(0,t\right)<T_f$, the estimation error is bounded in the L^2 norm.
Proof: Directly follows from Theorem 3. □

This leads us to the following conjecture for an output-feedback controller design.

Conjecture 2. Let $\hat{T}\left(x,t\right)$ and $\hat{s}\left(t\right)$ be the estimates of the plant $T\left(x,t\right)$ and $s\left(t\right)$ using the output injection described in Corollary 1. Let the plant be controlled using the certainty equivalence method, i.e. calculating control law (10) or (18) based on the estimates. Then the reference error $\tilde{T}\left(x,t\right)$ converges to an ε-neighborhood of zero reference error in the L^2 norm.

Although this conjecture is unproven, it is supported by the simulation results, given in the next section.

3.6. Simulation Results: The following simulation results use the parameters in Table 1. These are based on the thermal properties of ULC (ultra-low carbon) steel. The initial conditions are shown in Figure 7. The simulations employ an enthalpy-based method to model solidification, rather than an actual moving boundary. The simulation code was verified against an analytical solution to the Stefan problem from [35], and matched. The controlled simulations were found to be very noisy, as seen in the accompanying figures, and a hard bound was put on the permitted control values. This also better corresponds to the continuous casting process constraints, as heat fluxes below zero and above the maximum available by the water spray cooling system cannot be achieved.

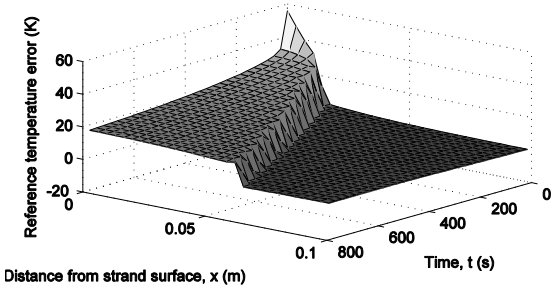

a) Reference temperature error $\tilde{T}\left(x,t\right)$

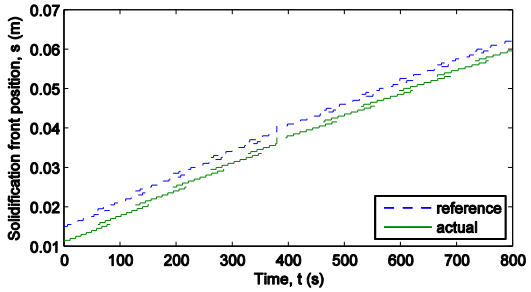

b) Solidification front positions $\bar{s}\left(t\right)$ and $s\left(t\right)$

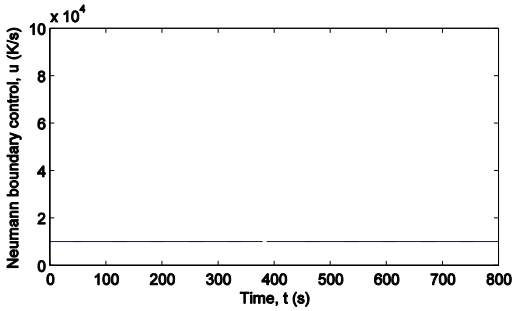

c) Neumann boundary control $u\left(t\right)$

Figure 8. Simulation results for system (5)-(6) with no control action.

Figure 8 shows the behavior of the system under open-loop control with $u\left(t\right)=\bar{u}\left(t\right)$ for all $t\ge 0$. In this case, the reference errors in both temperature and solidification front position appear to converge to constant, non-zero values. This approximates the current spray cooling state-of-the-art in most continuous casters, in which spray practices do not account for changes in superheat or mold heat removal.

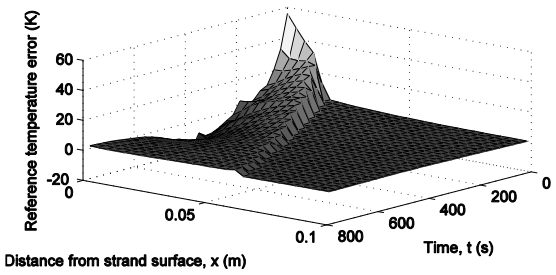

a) Reference temperature error $\tilde{T}(x,t)$

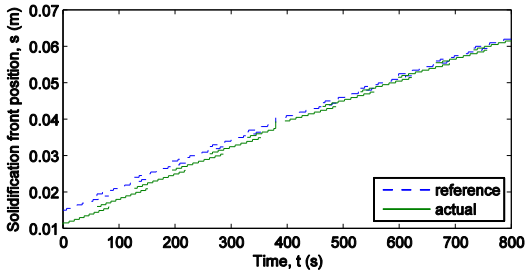

b) Solidification front positions $\bar{s}(t)$ and $s(t)$

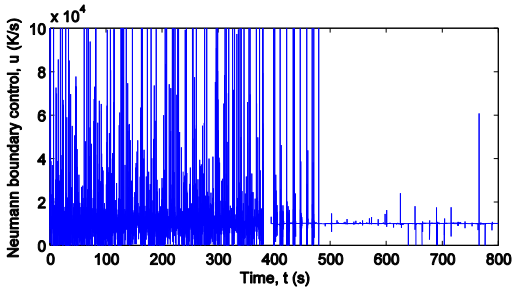

c) Neumann boundary control $u(t)$

Figure 9. Simulation results for system (5)-(6) under control law (10).

Figure 9 and Figure 10 show simulation results using control laws (10) and (18), respectively. Although Theorem 2 does not demonstrate convergence, the reference temperature error and solidification front position error do converge to zero in both simulations. Similarly, although convergence for the saturated control laws was not proven for either of these two control laws, the simulations demonstrate that the bounded control values still allow for good convergence. We conjecture that the errors converge for initial temperatures in a neighborhood of the initial reference temperature in some norm.

Finally, Figure 11 shows an implementation of the output-feedback control method described in Conjecture 2 using an estimator with initial condition $\hat{T}(x,0) = \bar{T}_0$ from Figure 7.

Again, although convergence was not proved, the reference temperature error appears to be converging to 0. We further note that the initial conditions in Figure 7

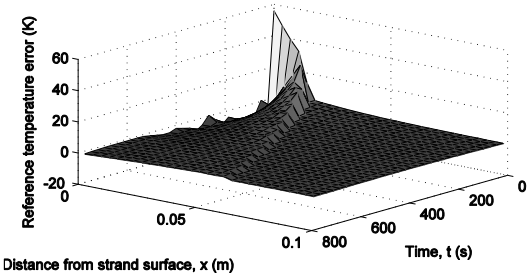

a) Reference temperature error $\tilde{T}(x,t)$

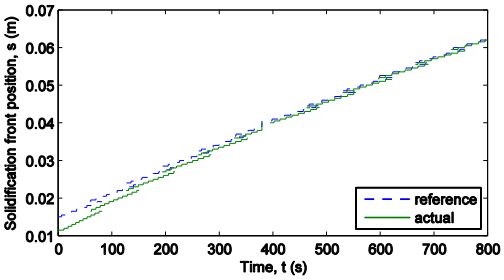

b) Solidification front positions $\bar{s}(t)$ and $s(t)$

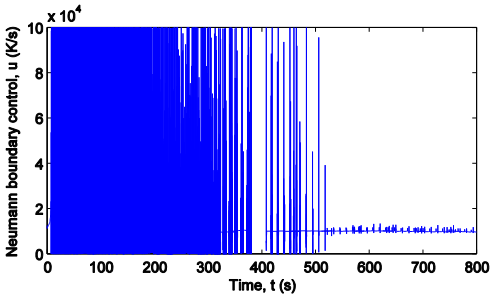

c) Neumann boundary control $u(t)$

Figure 10. Simulation results for system (5)-(6) under control law (18).

do not satisfy assumption (A4), which suggests that we could relax the hypotheses for Theorem 3.

4. Elimination of Distortion in Mold Oscillation System: In this section, the distortion problem in mold oscillation system, described in the introduction, is analyzed and an approach to resolve it is discussed.

4.1 Testbed of Mold Oscillation System and Problem Statement: To carry out experiments, a testbed of the mold oscillation system was built at Nucor Steel, Decatur. The testbed (Figure 12) has a hinged hollow beam that supports a heavy mass (~2500 Kgs), resembling a mold, on one end and has a servo actuator located at the other end. It exhibits the submultiples phenomenon present in the mold oscillation system, described in the introduction, albeit more pronounced. The first resonance frequency of the beam is 9.65 Hz. When the beam is driven by the actuator at 4.8 Hz, the mold displacement profile is severely distorted.

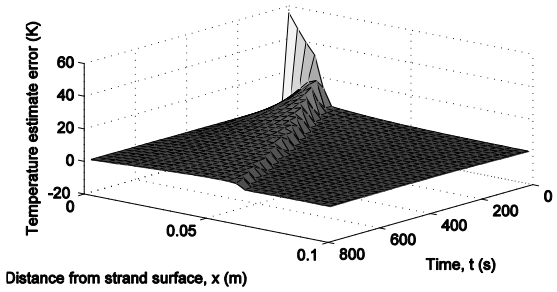

a) Temperature estimation error $T(x,t)-\hat{T}(x,t)$

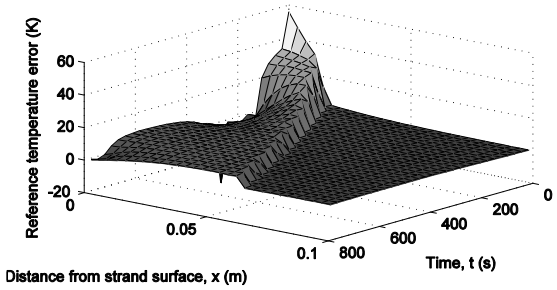

b) Reference temperature error $\tilde{T}(x,t)$

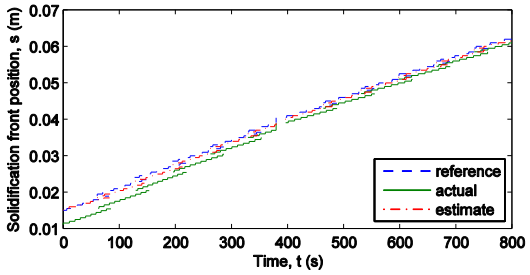

c) Solidification front positions $\bar{s}(t)$, $\hat{s}(t)$, and $s(t)$

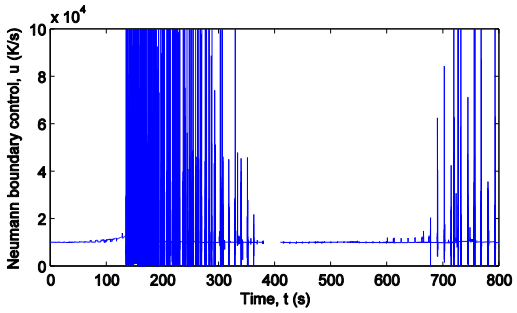

d) Neumann boundary control $u(t)$

Figure 11. Simulation results for system (5)-(6) under output-feedback with control law (18) based on estimator, as in Conjecture 2.

Figure 13 shows the testbed piston and the mold displacement profiles with servo under proportional feedback with a controller gain 2. The reference to the piston is a sinusoid of 3 mm magnitude and 4.8 Hz frequency. The distortion in the mold displacement is clearly visible, while the piston displacement seems to track the reference perfectly. The magnitude spectrum of the two signals shown in Figure 14 reveals, however, a small peak of about 0.04 mm at 9.6 Hz, which is twice the reference frequency, in the piston displacement. It was conjectured that being near the beam resonance frequency, this peak - a manifestation of the nonlinear servo dynamics - is amplified by the beam, yielding distortion at the mold end. Experiments verified that when the piston displacement was a sinusoid of 0.05 mm magnitude and 9.65 Hz frequency, the mold displacement magnitude was about 1.5 mm, which matches well the magnitudes of peaks in Figure 14. It is therefore expected that elimination of sinusoids near resonance frequency in the piston displacement signal will ensure distortion free mold displacement. Hence, the reference and the actual piston displacements are taken to be the input and output, respectively, for controller design in this paper.

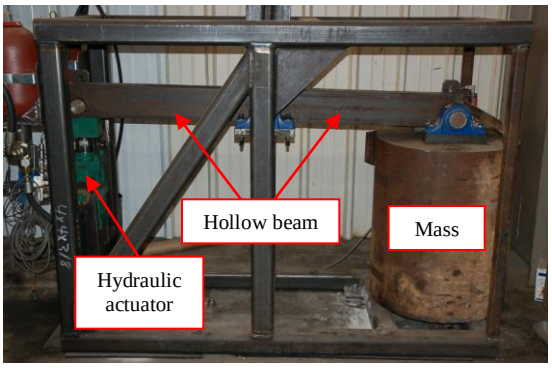

Figure 12. Picture of the mold oscillation system testbed

Electro-hydraulic servos, though inherently nonlinear, are designed to exhibit stable predominantly linear behavior in a nominal range of operation under feedback, implemented typically in the form of a P or a PI controller [36-38]. The effect of the beam on the piston in the operating range is mostly linear as well, making a linear system perturbed by small nonlinearity a plausible model for the input-output (reference - actual piston position) behavior of the servo system/testbed. This is confirmed, both in simulations and experiments, by the absence of any large nonlinear effects at the actuator output. Based on the above discussion the following *problem statement* is formulated:

Given a stable closed-loop system exhibiting perturbed linear dynamics that tracks the input sinusoid of frequency ω, but has the output containing small magnitude higher harmonics of ω due to nonlinear effects, augment the loop with a suitable filter so that

the harmonic at ω_r *in the output is eliminated without affecting the closed-loop stability and the tracking at frequency* ω. *Here* ω_r *is a specific integer multiple of* ω.

This problem is addressed in Section 4.3. In the application presented in this paper, ω_r is the first resonance frequency of the beam. The effect of small amplitude higher harmonics at frequencies other than ω_r on the beam is negligible and is omitted from consideration.

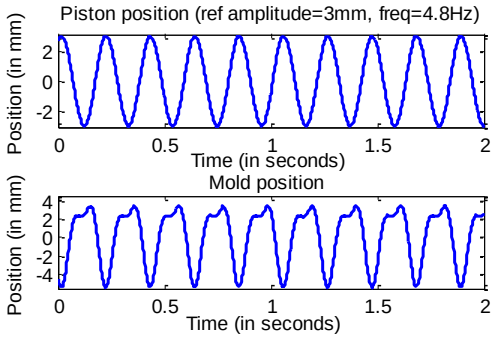

Figure 13. Experimental result: piston and mold position with piston reference at 4.8 Hz

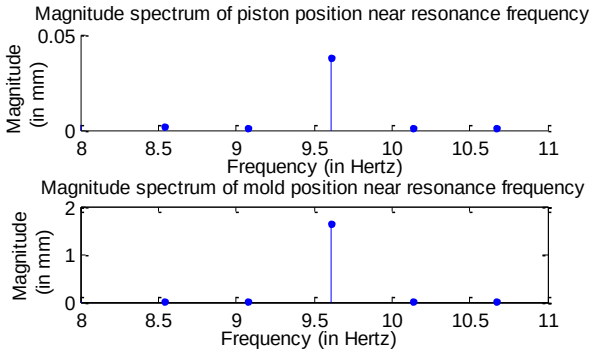

Figure 14. Experimental result: magnitude spectra of piston and mold position near resonance frequency

4.2 Coupled servo-beam model and simulations: Although not used as the basis of the proposed controller design, the models presented in below help understand the problem phenomenology, demonstrate the efficacy of the controller proposed, and carry out controller refinement under limited testbed access

4.2.1 Electro-hydraulic servo model:

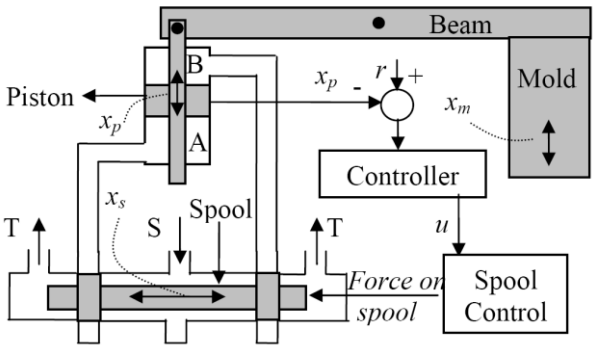

Figure 15. Schematic of the servo setup

A layout of the coupled servo and beam system is shown in Figure 15, where 'S' and 'T' refer to the supply of the pressurized fluid and the fluid on the tank side, respectively. The hydraulic actuator functions as follows [36, 38]. When the spool moves to the right, 'S' is connected to chamber 'B' and the piston is pushed down. When the spool moves to left, 'S' is connected to chamber 'A' and the piston is pushed up. Hence, the appropriate motion of the spool can cause the piston to oscillate. The servo system typically functions in the closed loop. The error between the desired and the actual piston position is used to control the spool position. Piston position x_p is governed by the equation

$$m_p\ddot{x}_p + b\dot{x}_p = (P_A - P_B)a_p - m_p g + F_B \qquad (22)$$

where m_p, b, P_A, P_B, a_p, g, F_B stand for the piston mass, damping, pressure in chamber 'A', pressure in chamber 'B', piston area, gravity, and force from the beam, respectively. When x_p is zero, chambers 'A' and 'B' have equal volumes. The pressures in chambers 'A' and 'B' are governed by

$$\dot{P}_A = \beta\left(q_A - a_p\dot{x}_p\right)\Big/\left(V_A + a_p\left(L + x_p\right)\right),$$
$$\dot{P}_B = \beta\left(-q_B + a_p\dot{x}_p\right)\Big/\left(V_B + a_p\left(L - x_p\right)\right). \qquad (23)$$

where β, q_A, q_B, V_A, V_B, L are bulk modulus of the actuator fluid, flow rates into chamber 'A' and out of chamber 'B', volumes of tubes connected to chambers 'A' and 'B' and half the stroke length of the piston, respectively. Assuming turbulent flow conditions, the flow rates q_A and q_B are given by

$$q_A = \begin{cases} c(d - x_s)\sqrt{P_s - P_A}, & x_s < -d, \\ c(d - x_s)\sqrt{P_s - P_A} & \\ -c(x_s + d)\sqrt{P_A - P_t}, & -d < x_s < d, \\ -c(x_s + d)\sqrt{P_A - P_t}, & x_s > d, \end{cases} \quad \text{and}$$

$$q_B = \begin{cases} c(d - x_s)\sqrt{P_B - P_t}, & x_s < -d, \\ c(d - x_s)\sqrt{P_B - P_t} & \\ -c(x_s + d)\sqrt{P_s - P_B}, & -d < x_s < d, \\ -c(x_s + d)\sqrt{P_s - P_B}, & x_s > d, \end{cases} \quad (24)$$

$$c = c_d w\sqrt{2/\rho}$$

where c_d, w, ρ, d, P_s, P_t, x_s are the effective discharge coefficient, width of port for fluid flow between chambers 'A'/'B' and 'S'/'T', density of the fluid, spool underlap length, supply pressure, tank pressure, and spool position, respectively. The spool position dynamics including the spool control is assumed to be governed by a second order system:

$$\ddot{x}_s + 2\zeta_s\omega_s\dot{x}_s + \omega_s{}^2 x_s = \omega_s{}^2 u \quad (25)$$

Here u is the input generated by a controller using error between x_p and desired reference signal r, as seen in Figure 15. Typically, a proportional control law

$$u = k(x_p - r) \quad (26)$$

is used where k is the proportional gain. In Figure 15 x_m is the mold position. Nominal values of the parameters are shown in the appendix.

4.2.2 Beam model: The hollow beam in the testbed is modeled as two beams attached at the hinge, each using Timoshenko beam model consisting of two coupled second order PDEs [39]. The coordinate along the length of the beams is x. The beams are coupled via the boundary conditions at the hinge location $x = 0$ that ensure that the torque and angular displacement at this location are identical. Thus, the model of the hinged beam of length $2l$ shown in Figure 16, with the vertical and the angular displacements to the left and to the right of the hinge denoted by (y_L, ψ_L) and (y_R, ψ_R), respectively, is given by a set of 4 coupled PDEs of the form

$$m_b\frac{\partial^2 y_L}{\partial t^2} + \gamma_y\frac{\partial y_L}{\partial t} = \frac{\partial}{\partial x}\left(k'Ga_b\left(\frac{\partial y_L}{\partial x} - \psi_L\right)\right) - m_b g,$$

$$\frac{I}{a_b}m_b\frac{\partial^2 \psi_L}{\partial t^2} + \gamma_\psi\frac{\partial \psi_L}{\partial t} = \frac{\partial}{\partial x}\left(EI\frac{\partial \psi_L}{\partial x}\right) + k'Ga_b\left(\frac{\partial y_L}{\partial x} - \psi_L\right),$$

$$m_b\frac{\partial^2 y_R}{\partial t^2} + \gamma_y\frac{\partial y_R}{\partial t} = \frac{\partial}{\partial x}\left(k'Ga_b\left(\frac{\partial y_R}{\partial x} - \psi_R\right)\right) - m_b g,$$

$$\frac{I}{a_b}m_b\frac{\partial^2 \psi_R}{\partial t^2} + \gamma_\psi\frac{\partial \psi_R}{\partial t} = \frac{\partial}{\partial x}\left(EI\frac{\partial \psi_R}{\partial x}\right) + k'Ga_b\left(\frac{\partial y_R}{\partial x} - \psi_R\right).$$

The mold dynamics is part of the boundary condition of the right beam at $x = l$. The boundary conditions are

$$y_L(-l) = x_p(t),\ EI\frac{\partial \psi_L(-l)}{\partial x} = 0,\ y_L(0) = 0,\ y_R(0) = 0,$$

$$\psi_L(0) = \psi_R(0),\ EI\frac{\partial \psi_L(0)}{\partial x} = EI\frac{\partial \psi_R(0)}{\partial x},\ EI\frac{\partial \psi_R(l)}{\partial x} = 0,$$

$$k'Ga_b\left(\frac{\partial y_R(l)}{\partial x} - \psi_R(l)\right) + Mg + M\frac{\partial^2 y_R(l)}{\partial t^2} + \gamma_m\frac{\partial y_R(l)}{\partial t} = 0.$$

In the equations m_b, a_b, G, E, I, γ_y / γ_ψ, γ_m, k', M stand for mass of beam per unit length, area of cross section of beam, shear modulus, Young's modulus, moment of inertia of beam, beam transverse/angular displacement damping, mold damping, shear constant, and mold mass. The nominal values of the parameters are presented in the appendix. The coupling between the nonlinear actuator and the beam is via the piston displacement entering the boundary condition for the left beam and the force F_B from the beam acting on the piston where

$$F_B = k'Ga_b\left(\frac{\partial y_L(-l)}{\partial x} - \psi_L(-l)\right). \quad (27)$$

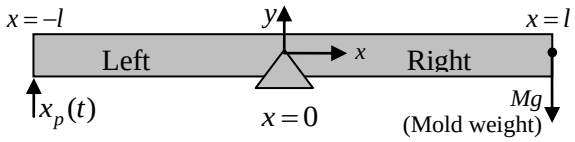

Figure 16. Beam Schematic

4.2.3 Simulation results

Simulation of the servo system in Figure 15 is performed using nominal parameter values. For the beam, except the value of I, which is reduced by 15% to match the experimental resonance frequency of the beam in the testbed, and the value of damping coefficients, which are tuned to match experimental amplification at resonance, nominal values for other physical parameters are those obtained using the measured dimensions of the beam. Some of the parameter values have been specifically obtained for the servo valve and actuator used in the testbed. Other values are obtained from references [40]. The initial chamber pressures are set at $P_A = P_B = 50\,P_t$. All other initial conditions are zero.

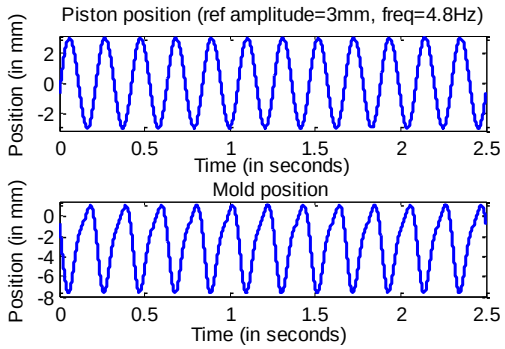

Figure 17. Simulation result: piston and mold position with piston reference at 4.8Hz

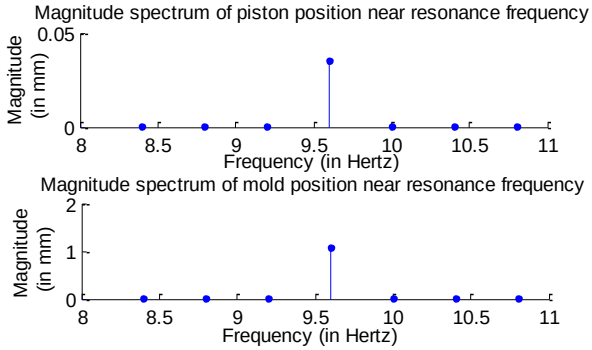

Figure 18. Simulation result: magnitude spectra of piston and mold position around resonance frequency

The servo simulation, which must run in closed loop, uses a proportional controller, with the value of u in eq. (25) given as $u = 0.6\left(x_p - r(t)\right)$ where $r(t)$ is a sinusoid of 3 mm magnitude and 4.8 Hz frequency. Figure 17 shows the mold position distortions similar to those in Figure 13, although not identical due to some plant/model mismatch. These distortions occur due to the nonlinear characteristics of the actuator that give rise to small amplitude sinusoid of frequency 9.6 Hz in the piston position, which excites the beam resonance. As in the experimental case, this is confirmed using spectral analysis of the simulated piston and mold position data (Figure 18). Therefore, the model presented adequately exhibits the submultiples problem and can be used as a platform for testing control strategies.

4.3 Controller design: Tracking and rejection of periodic signals with zero steady state error based on internal model principle [41] places the generator of the signal into the stable closed-loop system. This approach has been used in [42-45] and [46-48] for linear and nonlinear plants, respectively. In [47] internal model principle is utilized to eliminate undesirable periodic signal generated internally by a nonlinearly perturbed linear plant. In these works the plant model is assumed to be known. The approach in this work addresses rejection of an internally generated sinusoid of angular frequency ω_r assuming no knowledge of the plant and measuring only its forward path gain at ω_r .

The proposed solution in this work consists in augmenting the closed loop system Figure 19 with a filter to obtain the augmented system (Figure 20). The stability of the augmented system is guaranteed if the perturbation is small and if the unaugmented system forward path gain at frequency ω_r , further referred to for brevity as g_{KP} , satisfies a certain bound condition (given by (29)). Stability of the augmented loop ensures the rejection of sinusoidal disturbance at a single frequency, ω_r , from the given stable nonlinearly perturbed linear system while leaving the closed-loop response at frequencies away from ω_r nearly unaffected.

To formulate Theorem 1 which presents the controller, consider the system shown in Figure 19, referred to as the unaugmented system, where *P* is a nonlinear plant, *K* is a controller that stabilizes the loop, *r* is the reference input, and *y* is the output.

Theorem 1: Assume that the closed loop system in Figure 19 is described by a perturbed linear model:

$$\dot{x} = A_{cl}x + B_{cl}u + \varepsilon g(x), \qquad y = C_{cl}x, \qquad (28)$$

where A_{cl} *is Hurwitz and* $\varepsilon g(x)$ *is a small nonlinear perturbation. Let the unaugmented system forward path gain at* ω_r *, satisfy the condition*

$$\left|1/(1+g_{KP})\right| < 1. \qquad (29)$$

Next consider the feedback system shown in Figure 20, further referred to as the unpartitioned augmented system. For an appropriate choice of the linear stable transfer function F *, if* ε *is small, the unpartitioned augmented system tracks the input sinusoid of frequency* ω *and possibly contains small magnitude higher harmonics of* ω *induced by the nonlinear perturbation, but the harmonic at frequency* ω_r *is asymptotically eliminated from its output .*

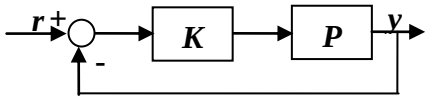

Figure 19. Block diagram of the unpartitioned unaugmented system

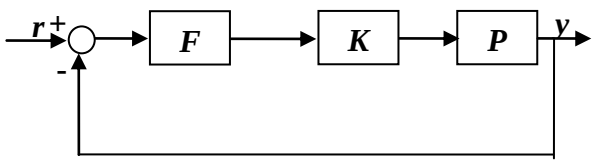

Figure 20. Block diagram of the unpartitioned augmented system

4.4 Numerical and experimental validation of the controller

4.4.1 Numerical controller validation: The controller of Theorem 1 is applied to the computational model of the testbed, presented in Section 4.2 to eliminate the distortions exhibited by the mold position in Figure 17. To verify the validity of assumption *B3*, the reference is chosen to be a sinusoid at frequency 9.65 Hz and magnitude 0.05 mm, and $|1/(1+g_{KP})|$ is calculated. As in Section 4.2, a proportional controller with a gain of 0.6 is used and simulations indicate that $|1/(1+g_{KP})|<1$. To test the scheme, $r(t)$ is chosen to be a sinusoid of magnitude 3 mm and frequency 4.8 Hz. A suitable filter is introduced as in Theorem 1. Comparing Figure 21 with Figure 17, the distortions in the mold position are seen to be dramatically reduced. Further on, examining Figure 22 and Figure 18 reveals that this reduction is attained through the drastic reduction of the magnitude of sinusoid at frequency 9.6 Hz contained in piston position. It is also seen that the augmentation of the closed loop has minimal effect on the system response at frequencies away from 9.6 Hz, as stated in Theorem 1.

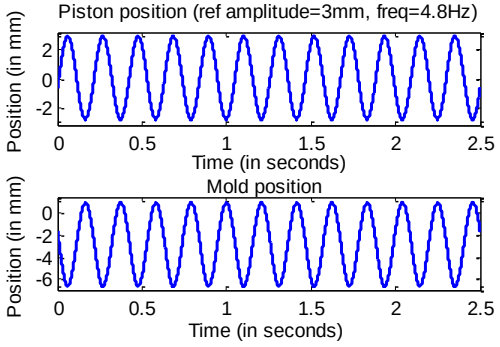

Figure 21. Simulation result: piston and mold position with reference at 4.8 Hz with augmented closed loop

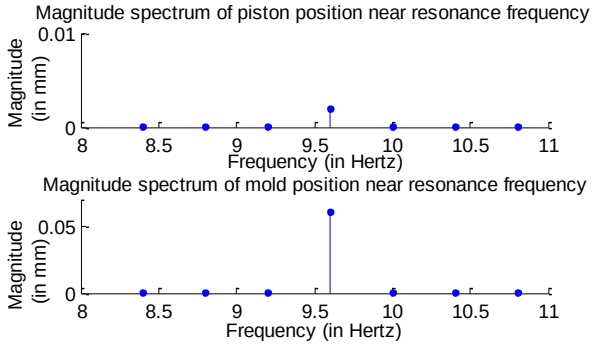

Figure 22. Simulation result: Magnitude spectra of piston and mold position near resonance frequency with augmented closed loop (magnitude at 9.6 Hz in mold position reduced by a factor of 17 compared to Figure 18)

4.4.2 Experimental controller validation: The control scheme of Theorem 1 was implemented on the testbed using NI LabVIEW® FPGA setup. The controller was implemented digitally, with a sampling interval of 1 millisecond, adequate for the largest frequency of interest, 9.6 Hz. The data was recorded with a sampling interval of 2 milliseconds.

The controller validation was carried out in three steps. In step one, the estimate of g_{KP} at ω_r for the unaugmented system under proportional feedback with a gain 2 (i.e. *k=2*) considered in Section 4.1 was obtained using a reference input of frequency 9.65 Hz and magnitude 0.05 mm. The corresponding gain g_{KP} did not satisfy the condition (29), and controller gain increase to 4 or 5 was required to obtain $|1/(1+g_{KP})|<0.7$, guaranteeing augmented system stability. But this was not done.

Instead, in step two, the augmented loop was tested in a wide frequency range: first, the proportional gain was set at 1, and the reference was chosen to be a sinusoid of 1 mm magnitude and 1 Hz frequency, resulting in instability. Increasing the proportional gain to 2, although not satisfying (29) as indicated above, permitted the augmented system to be operated safely over all amplitudes and frequencies of interest, making further gain increase unnecessary.

Step three demonstrated the efficacy of the controller: the reference input was chosen to be a sinusoid of magnitude 3 mm and frequency 4.8 Hz and the servo proportional feedback gain was set at 2, all as in Section 4.2 where large mold displacement distortion was observed. The filter was chosen based on Theorem 1. Figure 23 shows the corresponding piston and mold displacement profiles. The distortion in the mold displacement is seen to be much smaller compared to that of the unaugmented case shown in Figure 13. From Figure 24, it is seen that the magnitude of the sinusoid

at 9.6 Hz present in the piston position, and hence the mold position, is significantly reduced, compared to Figure 14. The piston position profiles in Figure 23 and Figure 13 are similar, since the augmentation of the closed loop has minimal effect on the response of the latter at frequencies away from 9.6 Hz. In Figure 24, the small peaks around 9.6 Hz are artifacts of data processing invisible in case of simulations and in Figure 14 due to much larger sampling rate and larger x-axis scale, respectively.

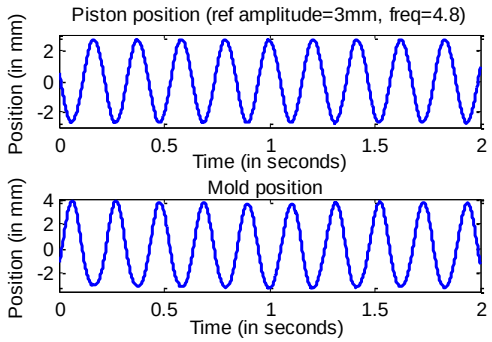

Figure 23. Experimental result: Piston and mold position with reference at 4.8 Hz with augmented loop

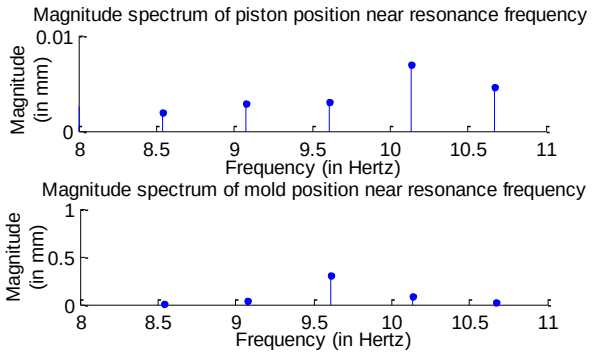

Figure 24. Experimental result: magnitude spectra of piston and mold position around resonance frequency after loop augmentation (magnitude at 9.6 Hz in mold position reduced by a factor of 5 compared to Figure 14)

5. Conclusion: This work addressed two methods of improving the control of cooling water sprays. A model-based PI control system, based on simulations and plant trials, represents a substantial improvement over current practices. It has the potential to reduce transverse cracking and allow the creation of better quality steel at higher casting speeds, increasing the steel supply for the customers and the profitability for the steel makers. The control law based on the Stefan problem is proven to provide temperature convergence throughout the strand, not at the surface. Although it is currently only conjecture, simulation results suggest that the control laws will ensure convergence under realistic operating conditions, including boundary sensing and limited actuation. This work also addressed the problem of rejecting an internally generated distortion in the mold oscillation system of some continuous casters, including those at Nucor Decatur. The procedure is demonstrated through simulations and experiments on the testbed. Future work involves applying these techniques to an industrial mold oscillation system.

Acknowledgments: This work is supported by NSF Grant # DMI-0900138, Continuous Casting Consortium of the University of Illinois at Urbana-Champaign, and Nucor Steel, Decatur, AL.

Appendix A. Technical Lemmas for Section 3:

Lemma 1. If $T(x,t)$ and $s(t)$ are solutions to the Stefan PDE (5)-(6) under assumptions (A1) and (A2) on some time interval for which $\varepsilon < s(t) < L-\varepsilon$ for some $\varepsilon > 0$, then $T(x,t)$ has infinite spatial derivatives.

Proof: Consider the change of variables

$$\xi := x / s(t),$$

$$\theta(\xi,t) := T(s(t)\xi,t) - T(0,t) + \xi\left(T(0,t) - T_f\right).$$

θ will solve the following linear time varying PDE:

$$\theta_t = \frac{a}{s^2}\theta_{\xi\xi} + \frac{\xi \dot{s}}{s}\theta_\xi - \frac{\xi \dot{s}}{s}\left(T(0) - T_f\right) + (\xi - 1)T_t(0),$$

$$0 < \xi < 1, \quad \theta(0,t) = \theta(1,t) = 0.$$

Under the assumptions, this PDE is uniformly parabolic in time, and the coefficients are infinitely differentiable in the spatial variable ξ. Therefore, by Theorem 3.10, p.72 in [49], θ is infinitely differentiable with respect to ξ, and consequently T is infinitely differentiable with respect to x on this interval and $0 < x < s(t)$. A similar change of variables can be made for the liquid phase. □

Lemma 2. $W^{1,2}(0,L)$, the Sobolev space of functions with weak first derivatives bounded in the 2-norm, can be embedded compactly in $C^0(0,L)$, the space of continuous functions under the usual supremum norm.

Proof: This proof is a slight extension of the remark following the Rellich-Kondrachov theorem in [50]. From Theorem 5.5, p. 269 in [50], we immediately have that $W^{1,2}(0,L)$ can be continuously embedded in $C^{0,\gamma}(0,L)$, the space of Holder continuous functions with coefficient $\gamma = 1 - 1/2 = 1/2$. Then, consider any bounded subset of $C^{0,\gamma}(0,L)$, i.e.

$\left\{ f \in C^{0,\gamma}(0,L) : \|f\|_{C^{0,\gamma}(0,L)} \le M \right\}$. Then for $\forall \varepsilon > 0$, if $|x-y| < \delta := (\varepsilon / M)^{1/\gamma}$,

$$|f(x)-f(y)| / |x-y|^{\gamma} \le M \Rightarrow |f(x)-f(y)| \le M |x-y|^{\gamma} \le M \left((\varepsilon / M)^{1/\gamma} \right)^{\gamma} = \varepsilon.$$

Therefore, the functions in this set are uniformly equicontinuous, and by the Ascoli-Arzela criterion (see, e.g. Appendix C.7 in [50]), the set is precompact in $C^0(0,L)$. Thus, we have $W^{1,2}(0,L)$ continuously embedded in $C^{0,\gamma}(0,L)$, compactly embedded in $C^0(0,L)$. Therefore, $W^{1,2}(0,L)$ is compactly embedded in $C^0(0,L)$. □

Appendix B. Nominal values of the parameters used in simulations in Section 4

Variable	Nominal value	Units
m_p	2	Kgs
b	1000	N.sec/m
a_p	0.0046	m^2
g	9.8	m/sec^2
β	$1.5x10^9$	Pa
V_A	$4.7113x10^{-5}$	m^3
V_B	$7.0464x10^{-5}$	m^3
L	0.015	m
c	$3x10^{-4}$	-
d	$1.27x10^{-6}$	m
P_s	20684250	Pa
P_t	206840	Pa
m_b	69.256	Kg/m
a_b	0.0088	m^2
G	$7.7\ x10^{10}$	Pa
E	$2\ x10^{11}$	Pa
I	$1.9204\ x10^{-5}$	m^4
γ_y	10	Kg/m/sec
γ_ψ	10	Kg.m/sec
γ_m	2	Kg/sec
k'	0.83	-
M	2250	Kgs
l	0.88	M
ζ_s	0.6	-
ω_s	255	rad/sec

References

[1] J. K. Brimacombe, et al., "Spray Cooling in Continuous Casting," in *Continuous Casting*, pp. 105-123. Iron and Steel Society, Warrendale, PA. 1984.

[2] M. M. Wolf, *Continuous Casting: Initial Solidification and Strand Surface Quality of Peritectic Steels*. Vol. 9. 1997, Warrendale, PA: Iron and Steel Society. 1-111.

[3] K. Okuno, et al., Iron Steel Eng. vol. 12, pp. 34-38. 1987.

[4] K.-H. Spitzer, et al., Iron Steel Inst. Jpn. vol. 32, pp. 848-856. 1992.

[5] S. Barozzi, P. Fontana, and P. Pragliola, Iron Steel Eng. vol. 11, pp. 21-26. 1986.

[6] B. Lally, L. Biegler, and H. Henein, Met. Trans. B. vol. 21B, pp. 761-770. 1990.

[7] K. Dittenberger, et al. "DYNACS Cooling Model - Features and Operational Results." in *VAI 7th International Continuous Casting Conference*. Linz, Austria, 1996.

[8] R. A. Hardin, et al., "A Transient Simulation and Dynamic Spray Cooling Control Model for Continuous Steel Casting," Metal. & Material Trans. vol. 34B, pp. 297-306. 2003.

[9] S. Louhenkilpi, et al. "On-Line Simulation of Heat Transfer in Continuous Casting of Steel." in *2nd Int. Conference on New Developments in Metallurgical Process Technology*. Riva del Garda, Italy, 19-21 Sept, 2004, 2004.

[10] K. Zheng, et al. "Design and Implementation of a Real-time Spray Cooling Control System for Continuous Casting of Thin Steel Slabs,." in *AISTech 2007, Steelmaking Conference Proceedings,* . Indianapolis, IN, 2007.

[11] B. G. Thomas, et al., "GOALI: Online Dynamic Control of Cooling in Continuous Casting of Thin Steel Slabs," in *Proceedings of 2009 NSF CMMI Engineering Research and Innovation Conference*, pp. 16p. National Science Foundation: Honolulu, Hawaii, June 22-25, 2009. 2009.

[12] Bryan Petrus, et al., "Real-Time Model-Based Spray-Cooling Control System for Steel Continuous Casting," Metals and Materials Transactions B. vol. to appear.

[13] B. Petrus, et al. "Implementation of a Real-Time Model-Based Spray-Cooling Control System for Steel Continous Casting." in *TMS 2011 Annual Meeting & Exhibition*. San Diego, CA, 2011.

[14] C. Saguez, "Optimal control of free boundary problems," in *System Modelling and Optimization*, pp. 776-788. Springer Berlin: Heidelberg. 1986.

[15] P. Neittaanmaki and D. Tiba, *Optimal Control of Nonlinear Parabolic Systems: Theory, Algorithms, and Applications*. Pure and Applied Mathematics. 1994, New York: Marcel Dekker.

[16] W. B. Dunbar, et al. "Boundary control of a nonlinear Stefan problem." in *42nd IEEE Conference on Decision and Control*, 2003.

[17] S. Kang and N. Zabaras, "Control of the freezing interface motion in two-dimensional solidification processes using the adjoint method," International Journal for Numerical Methods in Engineering. vol. 38, pp. 63-80. 1995.

[18] M. Hinze and S. Zigenbalg, "Optimal control of the free boundary in a two-phase Stefan problem," Journal of Computatinal Physics. vol. 223, pp. 657-84. 2007.

[19] K.-H. Hoffmann and J. Sprekels, "Real-time control of a free boundary problem connected with the continuous casting of steel," in *Optimal Control of Partial Differential Equations*. Birkhauser: Basel, Switzerland. 1984.

[20] P. Colli, M. Grasselli, and J. Sprekels, "Automatic control via thermostats of a hyperbolic Stefan problem with memory," Applied Mathematics and Optimization. vol. 39, pp. 229-255. 1999.

[21] B. Furenes and B. Lie, "Solidification and control of a liquid metal column," Simulation Modelling Practice and Theory. vol. 14, pp. 1112-1120. 2006.

[22] E. S. Szerekes, "Overview of mold oscillation in continuous casting," *Iron and Steel Engineer (USA)*. vol. 73, pp. 29-37. 1996.

[23] Y. Meng and B. G. Thomas, "Heat Transfer and Solidification Model of Continuous Slab Casting: CON1D," Metal. & Material Trans. vol. 34B, pp. 685-705. 2003.

[24] Y. M. Won and B. G. Thomas, "Simple Model of Microsegregation during Solidification of Steels," Metallurgical and Materials Transactions A (USA). vol. 32A, pp. 1755-1767. 2001.

[25] B. Santillana, B.G. Thomas, Arie Hamoen, Lance Hibbeler, Arnaud Kamperman, and Willem Van der Knoop, "Investigating Mould Heat Transfer in Thin Slab Casting with CON1D," Ironmaker and Steelmaker. vol. 5, pp. 51-63. 2008.

[26] Joydeep Sengupta, et al. "Utilization of CON1D at ArcelorMittal Dofasco's No. 2 Continuous Caster for Crater End Determination." in *AISTech 2009 Steelmaking Conference Proc.* St. Louis, MO, May 4-7, 2009, 2009.

[27] C. Edwards and I. Postlethwaitex. "Anti-windup and Bumpless Transfer Schemes." in *UKACC International Conference on CONTROL*, 1996.

[28] C. Brosilow and B. Joseph, *Techniques of Model-Based Control*. Prentice-Hall international series in the physical and engineering sciences. 2002, Upper Saddle River, NJ: Prentice Hall.

[29] Y. V. Orlov and M. V. Basin, "On Minmax Filtering Over Discrete-Continuous Observations,"

IEEE Transactions on Automatic Control. vol. 40, pp. 1623-1626. 1995.
[30] L. I. Rubinsteĭn, *The Stefan Problem*. Translations of Mathematical Monographs. Vol. 27. 1971, Providence, RI: American Mathematical Society.
[31] M. Krstic and A. Smyshlyaev, *Boundary Control of PDEs: A course on Backstepping Designs*. Advances in Design and Control. 2008, Philadelphia: SIAM.
[32] J. A. Walker, *Dynamical Systems and Evolution Equations: Theory and Applications*. 1980, New York: Plenum Press.
[33] S. C. Gupta, *The Classical Stefan Problem: Basic Concepts, Modelling and Analysis*. North-Holland Series in Applied Mathematics and Mechanics. Vol. 45. 2003, Amsterdam: Elsevier.
[34] A. M. Meirmanov, *The Stefan Problem*. De Gruyter Expositions in Mathematics. 1986, Berlin, Germany: Walter de Gruyter.
[35] J. A. Dantzig and C. L. Tucker, *Modeling in Materials Processing*. 2001, New York: Cambridge University Press.
[36] D. H. Kim and T.-C. Tsao, "A linearized electrohydraulic servovalve model for valve dynamics sensitivity analysis and control system design," *ASME Journal of Dynamic Systems, Measurement, and Control*. vol. 122, pp. 179-187. 2000.
[37] W. J. Thayer, *Transfer functions for moog servovalves*, in *Technical Bulletin 103*. 1965, Moog Inc. Controls division: East Aurora, NY.
[38] H. E. Merrit, *Hydraulic control systems*. 1967, NY: Wiley and Sons.
[39] L. Meirovitch, *Analytical methods in vibrations*. 1967: The Macmillan company.
[40] M. R. Sirouspour and S. E. Salcudean. "On the nonlinear control of hydraulic servo-systems." in *Proceedings of the 2000 IEEE International conference on Robotics and Automation*. San Fransisco, CA, 2000.
[41] B. A. Francis and W. M. Wonham, "The internal model principle for linear multivariable regulators," *Appl. Math. Optim.* vol. 2, pp. 170-194. 1975.
[42] S. Hara, et al., "Repetitive control system: A new type servo system for periodic exogenous signals," *IEEE Transactions on Automatic control*. vol. 33, pp. 659-668. 1988.
[43] M. Tomizuka, T.-C. Tsao, and K.-K. Chew, "Analysis and synthesis of discrete-time repetitive controller," *ASME Journal of Dynamic Systems, Measurement, and Control*. vol. 111, pp. 353-358. 1989.
[44] L. J. Brown and Q. Zhang, "Periodic disturbance cancellation with uncertain frequency," Automatica. vol. 40, pp. 631-637. 2004.
[45] T. J. Manayathara, T. C. Tsao, and J. Bentsman, "Rejection of Unknown Periodic Load Disturbances in Continuous Steel Casting Process Using Learning Repetitive Control Approach," IEEE Transactions on Control Systems Technology. vol. 4, pp. 259-265. 1996.
[46] T. Omata, S. Hara, and M. Nakano, "Nonlinear repetitive control with application to trajectory control of manipulators," *Journal of Robotic systems*. vol. 4, pp. 631-652. 1987.
[47] J. Ghosh and B. Paden, "Nonlinear repetitive control," *IEEE Trans. on Automatic control*. vol. 45, pp. 949-954. 2000.
[48] P. Lucibello, "Comments on “Nonlinear repetitive control”," *IEEE Trans. on Automatic control*. vol. 48, pp. 1470-1471. 2003.
[49] A. Friedman, *Partial Differential Equations of Parabolic Type*. 1964, Engtlewood Cliffs, NJ: Prentice-Hall, Inc.
[50] L. C. Evans, *Partial Differential Equations*. Graduate Studies in Mathematics. 1998, Providence, RI: American Mathematical Society.